CHANCE	**Title :** Deliverable D3.3 Results of experimental investigation of calorimetry applicability	Written:	List on Page 2		
		Organisation:	List on page 2	Version:	0
		Issued:	02nd April 2022	Page(s):	1

Characterization of Conditioned Nuclear Waste
for its Safe Disposal in Europe

Deliverable D3.3
Results of experimental investigation of calorimetry Applicability

CHANCE project
Work Package

Work programme topic addressed: "Research and innovation on the overall management of radioactive waste other than geological disposal"

Supply Chain Security topic

Task 3.2 Experimental Investigation

EC Grant Agreement number: H2020-755371

Start date of project: June 1, 2017   Duration: 58 months

Lead beneficiary of this deliverable:

Due date of deliverable: 02/04/2022

Project funded by the European Commission within the Horizon 2020 Program (2014-2020)		
Type		
R	Document, report excluding the periodic and final reports	
DEM	Demonstrator, pilot, prototype, plan designs	X
DEC	Websites, patents filling, press & media actions, videos, etc.	
OTHER	Software, technical diagram, etc.	
Dissemination level		
PU	PUBLIC, fully open, e.g. web	X
CO	CONFIDENTIAL, restricted under conditions set out in Model Grant Agreement	

CHANCE

CHANCE

Title : Deliverable D3.3

Results of experimental investigation of calorimetry applicability

Written:	List on Page 2		
Organisation:	List on page 2	Version:	0
Issued:	02nd April 2022	Page(s):	2

V #	Date	Type of revision	Author
0	04/04/2022	Published version	WP3

Deliverable Contributors

Authors

Partner	Name
CEA	Cédric Carasco
CEA	Bertrand Perot
SCK CEN	Bart Rogiers
SCK CEN	Sven Boden
SCK CEN	Alessandro Borella
SCK CEN	An Bielen
KEP	Christophe Mathonat
KEP IC	Andrea Francescon
KEP IC	Xavier Mettan
WUT	Wojciech Kubinski

Internal Reviewers

Partner	Name
Andra	Denise Ricard

Contents

CHANCE

Title : Deliverable D3.3

Results of experimental investigation of calorimetry applicability

Written: List on Page 2

Organisation: List on page 2   Version: 0

Issued: 02nd April 2022   Page(s):   5

Table of figures

CHANCE	**Title :** Deliverable D3.3 Results of experimental investigation of calorimetry applicability	Written:	List on Page 2		
		Organisation:	List on page 2	Version:	0
		Issued:	02nd April 2022	Page(s):	8

Table of Tables

CHANCE

Title : Deliverable D3.3

Results of experimental investigation of calorimetry applicability

Written: | List on Page 2

Organisation: | List on page 2 | Version: | 0

Issued: | 02nd April 2022 | Page(s): | 9

Glossary

Caption / Acronym	Description/Meaning
ANDRA	Agence nationale pour la gestion des déchets radioactifs
CHANCE	Characterisation of conditioned nuclear waste for its Safe Disposal in Europe
ESARDA	European Safeguards Research and Development Association
FRAM	Fixed energy, Response function Analysis with Multiple efficiencies
IEM	Infinite Energy Method
ISOCS	In Situ Object Counting System
KEPIC	KEP Innovation Centre
LVC	Large Volume Calorimeter
MCNP	Monte Carlo N-Particle code
PNMC	Passive Neutron Measurement Counting
PNCC	Passive Neutron Coïncidence Counting
RAD	Rossi-alpha distribution
RN	Radionuclide
SCK CEN	Belgian nuclear research centre
XPS	Extruded polystyrene

CHANCE

Title : Deliverable D3.3	Written:	List on Page 2	
Results of experimental investigation of calorimetry applicability	Organisation:	List on page 2	Version: 0
	Issued:	02nd April 2022	Page(s): 10

1 Executive Summary

1.1 Executive Factsheet

Who should read this deliverable? Who are the stakeholders concerned by this deliverable?	Why should s/he read this deliverable? What will s/he learn from this deliverable?	Which part of the content is most relevant for him / her?
End User Group	This document is presenting the results of experimental investigation of calorimetry applicability by CEA and SCK•CEN for Task 3.2.	Sections 3, 4, 5, 6

FIGURE 1 - EXECUTIVE FACTSHEET

1.2 Executive Summary

The CHANCE project aims to address the specific issue of the characterization of conditioned radioactive waste. The characterization of fully or partly conditioned radioactive waste is a specific issue because unlike for raw waste, its characterization is more complex and therefore requires more advanced non-destructive techniques and methodologies.

The objective of CHANCE is to further develop, test and validate techniques already identified that will improve the characterization of conditioned radioactive waste, namely those that cannot easily be dealt with using conventional methods. Specifically, the work on conditioned radioactive waste characterization technology focuses on:

- Calorimetry as an innovative non-destructive technique to reduce uncertainties on the inventory of radionuclides;
- Muon Tomography to address the specific issue of non-destructive control of the content of large volume nuclear waste;
- Cavity Ring-Down Spectroscopy (CRDS) as an innovative technique to characterize outgassing of radioactive waste.

The present report focuses on activities from Work Package 3 related to the development of the calorimetry. In the frame of the Task 3.2 "Experimental investigation", some measurements were carried out with mock-up waste drums at CEA Cadarache and SCK CEN with gamma spectrometry, passive neutron counting and using the calorimeter developed by KEP Technologies. SCK CEN also performed measurements with a 200 L real unconditioned waste drum. This document presents the results obtained with the different techniques and some MCNP modelling of the calorimeter in the framework of the performed experiments.

2 The 200 litres calorimeter with lowered detection limit

The CHANCE LVC presented in deliverable D3.2 [1] is based on a calorimetric principle using some measuring and reference sensors surrounding the sample to be studied (drum) and monitoring all the heat released by the sample.

The sensors are some Peltier elements generating a differential signal proportional to the deviation of the heat flux going through the measuring sensors from the one going through the reference sensors.
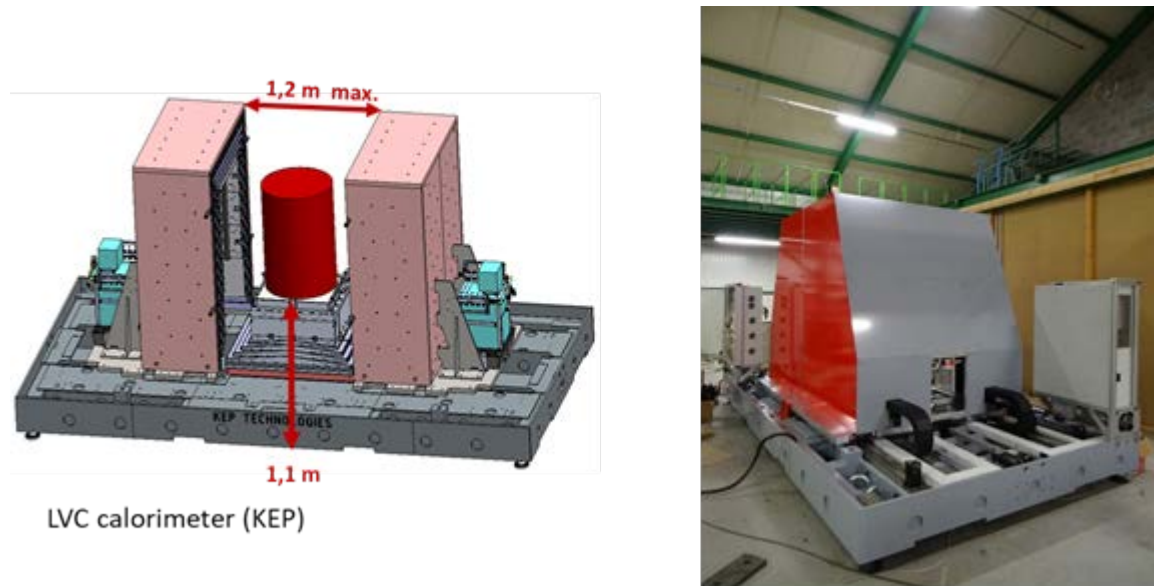
FIGURE 2 - CAD VIEW AND PHOTOGRAPH OF THE LVC CHANCE CALORIMETER

The LVC CHANCE calorimeter operates in the heat-flow-measurement mode. The sample inserted inside the measurement chamber generates heat as a consequence of its radioactivity. The reference block is kept at a constant-stable temperature and sensing Peltier elements convert the heat fluxes across different parts of the calorimeter into voltage signals V_i (either measuring or reference). Because the signal related to the heat flux is weak and subjected to various sources of noise (discussed further in this report), a *differential* measurement is implemented to significantly cancel out noise. In addition to the measurement cell, *ghost cells* are arranged in symmetrical configurations inside the calorimeter and act as reference cells (Figure 3). Simultaneous measurements of sample and reference voltages permit a differential cancellation of noise and offsets. As the calorimeter consists of two shells and the base, each of these parts contains its own measurement system and the output of the calorimeter at a given time is the sum of all three signals:

$$V_s = \sum_{l,c,r} (V_i^{\mathrm{MEAS}} - V_i^{\mathrm{REF}})$$

(2.1)

where *l*, *c* and *r* stand for the left, centre and right parts of the calorimeter. Where V_i^{meas} and V_i^{ref} are respectively signals registered by measuring sensors and reference sensors.
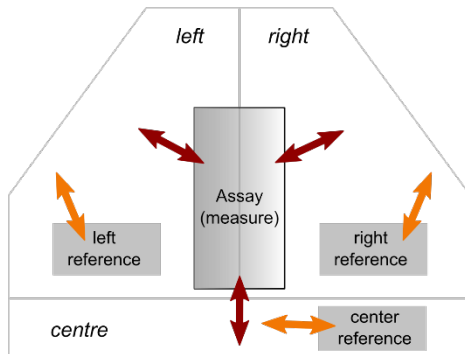
FIGURE 3 - THERMAL TRANSFERS BETWEEN THE NUCLEAR ASSAY AND THE LEFT, RIGHT AND CENTRE PARTS OF THE CALORIMETER (NOT TO SCALE). EACH ARROW DEPICTS HEAT FLUXES INSIDE THE CALORIMETER. THESE FLUXES GENERATE INDEPENDENT VOLTAGE SIGNALS V_i MEASURED BY AN ASSEMBLY OF PELTIER ELEMENTS. ALL THESE CONTRIBUTIONS ARE SUMMED ACCORDING TO EQ. (2.1) TO GIVE THE SIGNAL VOLTAGE V_s. THE RED ARROWS REPRESENT THE HEAT EMITTED BY THE DRUM. THE ORANGE ARROWS REPRESENT THE HEAT EMITTED BY THE REFERENCE CELLS

In order to precisely evaluate the heat flux generated by an assay, a "zero-signal" V_{BL} (baseline) of the calorimeter has to be recorded prior to measurements of active samples. Therefore, a preliminary measurement with e.g., an empty measurement chamber is performed, and the heat flux signal acquired at this step is called baseline. Only then, the main measurement can be done. After the measurement, the new baseline is recorded one more time to determine the average baseline $\bar{V}_{\mathrm{BL}}$. The quantity of interest – the voltage drop originating from heat generated by an assay - is calculated as the difference between the signal with loaded sample and the average baseline:

$$\Delta V_{\mathrm{net}} = V_s - \bar{V}_{\mathrm{BL}} \tag{2.2}$$

$$\bar{V}_{\mathrm{BL}} = \frac{V_{\mathrm{BL}\,1} + V_{\mathrm{BL}\,2}}{2} \tag{2.3}$$

ΔV_{net} only provides a relative indication on the heat generated by an active assay. Measurements of heat fluxes from Peltier elements thus require prior knowledge of the sensitivity of the sensors, so that the total heat generated by the sample W_{item} is:

$$W_{\mathrm{item}} = \frac{\Delta V_{\mathrm{net}}}{S} \tag{2.4}$$

where S (µV/mW) is the sensitivity of the calorimeter. In order to obtain a quantitative probe, the calibration of S is mandatory. This calibration procedure is performed employing special cells able to provide a controllable power. The so-called "Joule effect cells" (EJ cells) are containers with embedded resistor. The electrical power dissipated in these resistors is fully converted to heat, hence enabling precise knowledge of the power generated by the assay. As for the measurements described in this section, a baseline is acquired, after which step power is injected into the EJ cell and ΔV_{net} can be extracted.

The calorimeter is based on a principle patented with CEA [2]. It has been featured for 200 litres drum and a new temperature regulation system.

CHANCE

Title : Deliverable D3.3

Results of experimental investigation of calorimetry applicability

Written: List on Page 2

Organisation: List on page 2   Version: 0

Issued: 02nd April 2022   Page(s):   13
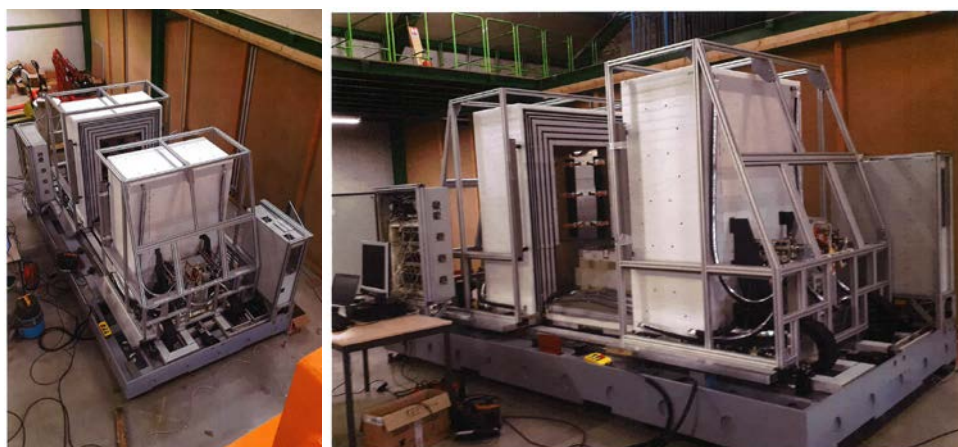
FIGURE 4 NEW CALORIMETER DEVELOPED BY KEP TO MEASURE 200 L WASTE DRUMS, DURING ITS MOUNTING.

3   Non-destructive measurements at CEA

At CEA Cadarache, two 200 L test drums equipped with instrumentation holes to place radioactive sources were initially selected [3]. One drum was filled with concrete to enhance limitations associated to both gamma spectrometry and neutron measurements relative to calorimetry and the other drum was filled with bitumen to enhance limitations associated to neutron measurements relative to gamma spectrometry and calorimetry. Unfortunately, the calorimeter breakdown during the first COVID 19 confinement episode allowed the full measurement of only the drum filled with concrete.

3.1   Gamma-ray spectrometry

3.1.1   Measurements

The gamma ray spectra associated to CEA plutonium samples have been measured in different positions inside the concrete drum with a 9% relative efficiency Broad Energy Germanium Detector (Canberra BEGe2020 [4]) placed in front of the drum and surrounded by lead shielding as shown in Figure 5. A 1.5 mm thick stain filter is also placed in front of the BEGe2020 to limit the count rate associated to X rays and low energy gamma rays (such as the 59.5 keV [241]Am gamma ray). The absolute detection efficiency of this detector is shown in Figure 6.

FIGURE 5 GAMMA SPECTROSCOPIC MEASUREMENT OF THE CONCRETE TEST DRUM WITH THE **LMN 9% HPGE** DETECTOR (LEFT) AND TOP VIEW OF THE CONCRETE TEST DRUM SHOWING THE HOLES IN WHICH A RADIOACTIVE SOURCE CAN BE PUT (RIGHT). NOTE: THE DRUM COLOUR IS BLACK DUE TO CALORIMETER OVERHEATING BUT ITS NATIVE COLOUR WAS RED, AS CAN BE SEEN IN FIGURE 16.
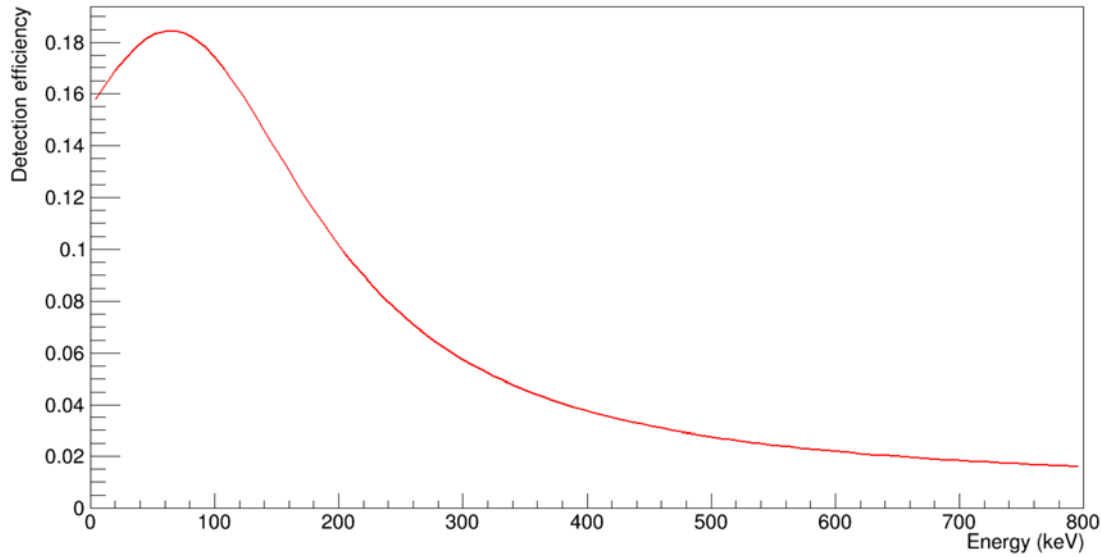
FIGURE 6 ABSOLUTE DETECTION EFFICIENCY OF THE HPGE DETECTOR USED FOR MEASURING PLUTONIUM GAMMA RAYS EXITING THE CONCRETE DRUM, WITH SOURCES PLACED AT 40 CM FROM THE HPGE.

3.1.2 Associated numerical studies

Taking into account plutonium self-absorption, the attenuation due to the concrete, the 5mm thick aluminium tubes that serves to put radioactive sources in the concrete drum (see Figure 5), the drum iron cat, the stain filter, as well as the attenuation of the plutonium iron cast and the plutonium self-attenuation, the expect number of counts seen by the BEGe2020 for a gamma ray with energy $E_{i,e}$ emitted from the plutonium sample is:

$$N(E_{i,e}) = M \cdot A_i \cdot f_i \cdot BR(E_{i,e}) \cdot T \cdot \frac{1 - e^{-\left(\frac{\mu}{\rho}\right)_{Pu}(E_{i,e}) \cdot \rho_{Pu} \cdot d_{Pu}}}{\left(\frac{\mu}{\rho}\right)_{Pu}(E_{i,e}) \cdot \rho_{Pu} \cdot d_{Pu}} \cdot e^{-\Sigma_{m=SiO_2, Al, Fe, Sn}\left(\frac{\mu}{\rho}\right)_m (E_{i,e}) \cdot \rho_m \cdot d_m} \cdot \frac{d\Omega}{4\pi} \cdot \varepsilon(E_{i,e})$$

With M the plutonium mass, A_i the specific activity of nucleus i, f_i the isotopic fraction of i, $BR(E_{i,e})$ the branching ratio for nuclei i to emit a gamma ray with energy $E_{i,e}$, $\left(\frac{\mu}{\rho}\right)_m (E_{i,e})$ the mass attenuation coefficient related to material m in the photon path, ρ_m the density of material m, d_m the thickness of material m, $d\Omega$ the solid angle sustained by the HPGe detector and $\varepsilon(E_{i,e})$ the full peak energy detection efficiency of the HPGe detector for a photon with energy $E_{i,e}$ shown in Figure 6. The concrete is considered to be made from SiO₂.

The previous formula is correct when the plutonium samples are placed on top of each other, which means that photons undergo self-absorption from only one of the plutonium samples. When the samples are placed one behind the others, relative to the detector, we have:

CHANCE

Title : Deliverable D3.3	Written:	List on Page 2		
Results of experimental investigation of calorimetry applicability	Organisation:	List on page 2	Version:	0
	Issued:	02nd April 2022	Page(s):	16

$$N(E_{i,e}) = M \cdot A_i \cdot f_i \cdot BR(E_{i,e}) \cdot T \cdot \frac{1}{P} \cdot \sum_{p=0}^{P} \frac{1-e^{-\left(\frac{\mu}{\rho}\right)_{Pu}(E_{i,e})\cdot\rho_{Pu}\cdot d_{Pu}}}{\left(\frac{\mu}{\rho}\right)_{Pu}(E_{i,e})\cdot\rho_{Pu}\cdot d_{Pu}} e^{-p\cdot\left(\frac{\mu}{\rho}\right)_{Pu}(E_{i,e})\cdot\rho_{Pu}\cdot d_{Pu}} \cdot e^{-(2p+1)\cdot\left(\frac{\mu}{\rho}\right)_{Fe}(E_{i,e})\cdot\rho_{Fe}\cdot d_{Fe}} \cdot$$

$$e^{-\sum_{m=SiO_2,Al,Fe,Sn}\left(\frac{\mu}{\rho}\right)_m(E_{i,e})\cdot\rho_m\cdot d_m} \cdot \frac{d\Omega}{4\pi} \cdot \varepsilon(E_{i,e}) \quad (3.1)$$

To comply with EURATOM regulations, no information can be delivered concerning the CEA plutonium samples that have been used for the CHANCE measurements. Therefore, to avoid revealing details related to the plutonium samples, the comparison between measurements and calculations is done by

comparing $\frac{N(E_{i,e})}{A_i \cdot f_i \cdot BR(E_{i,e}) \cdot T}$ and $\frac{1-e^{-\left(\frac{\mu}{\rho}\right)_{Pu}(E_{i,e})\cdot\rho_{Pu}\cdot d_{Pu}}}{\left(\frac{\mu}{\rho}\right)_{Pu}(E_{i,e})\cdot\rho_{Pu}\cdot d_{Pu}} \cdot \left(e^{-\sum_{m=SiO_2,Al,Fe,Sn}\left(\frac{\mu}{\rho}\right)_m(E_{i,e})\cdot\rho_m\cdot d_m}\right) \cdot \varepsilon(E_{i,e}) \cdot \frac{d\Omega}{4\pi}$ or $\frac{1}{P} \cdot$

$\sum_{p=0}^{P} \frac{1-e^{-\left(\frac{\mu}{\rho}\right)_{Pu}(E_{i,e})\cdot\rho_{Pu}\cdot d_{Pu}}}{\left(\frac{\mu}{\rho}\right)_{Pu}(E_{i,e})\cdot\rho_{Pu}\cdot d_{Pu}} e^{-p\cdot\left(\frac{\mu}{\rho}\right)_{Pu}(E_{i,e})\cdot\rho_{Pu}\cdot d_{Pu}} \cdot e^{-(2p+1)\cdot\left(\frac{\mu}{\rho}\right)_{Fe}(E_{i,e})\cdot\rho_{Fe}\cdot d_{Fe}} \cdot e^{-\sum_{m=SiO_2,Al,Fe,Sn}\left(\frac{\mu}{\rho}\right)_m(E_{i,e})\cdot\rho_m\cdot d_m} \cdot \frac{d\Omega}{4\pi} \cdot$

$\varepsilon(E_{i,e})$, depending on the way the samples are placed.

Such a comparison is shown when the plutonium samples are placed on top of each other in Figure 7, Figure 8 and Figure 9, when the samples are placed in peripheral position, half radius position and in the middle of the drum, respectively. When the plutonium samples are placed in the other configuration, the comparison between measurement and calculation is shown in Figure 10. To visualize the impact of concrete density uncertainty, which is responsible for most of the attenuation when the plutonium is positioned in the deepness of the drum, the figures include calculations with ±1% variations of the concrete nominal density which is ρ_{SiO2}=(2.48±0.03) g/cm³. The calculations are performed with the 129 keV, 203 keV, 345 keV and 414 keV gamma rays from ²³⁹Pu, ²⁴⁰Pu 160 keV gamma ray and ²⁴¹Pu 149 keV gamma ray.

At high energy, the agreement between the calculation and the experiment is satisfactory. However, modelling gamma ray attenuation at low energy is difficult and in particular, plutonium self-absorption are usually difficult to model [5], which could explain the observed discrepancies. In the case of Figure 7, for which the samples are near the drum iron wall, the measured concrete thickness was about 5 mm when looking from the top of the drum, see Figure 5. However, at this position, for such a small thickness the concrete granularity makes difficult a reliable thickness assessment.

One can notice that the measurement is very sensitive to the plutonium position. For example, there is a factor 200 for the amplitude of gamma rays above 300keV between peripheral position (Figure 7) and central position (Figure 9).

CHANCE

Title : Deliverable D3.3	Written:	List on Page 2	
Results of experimental investigation of calorimetry applicability	Organisation:	List on page 2	Version: 0
	Issued:	02nd April 2022	Page(s): 17
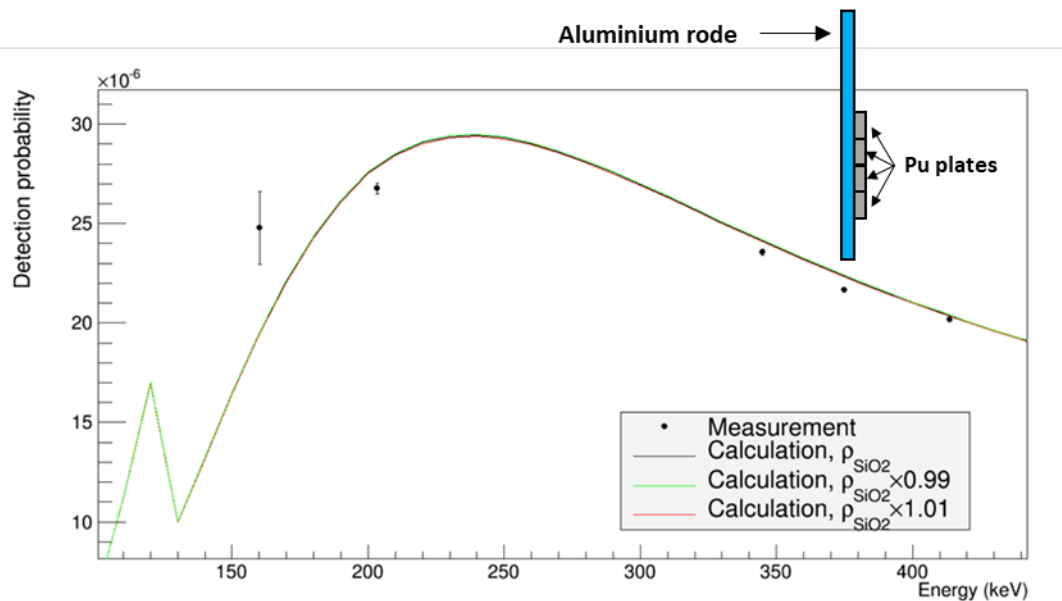
FIGURE 7 PROBABILITY OF DETECTING A PLUTONIUM GAMMA RAY EMITTED FROM THE PLUTONIUM SAMPLES AS A FUNCTION OF ENERGY, WHEN THE PLUTONIUM SAMPLES ARE PLACED AT THE PERIPHERY OF THE DRUM AND STACKED VERTICALLY ALONG AN ALUMINIUM RODE AS SHOWN IN THE DRAWING.
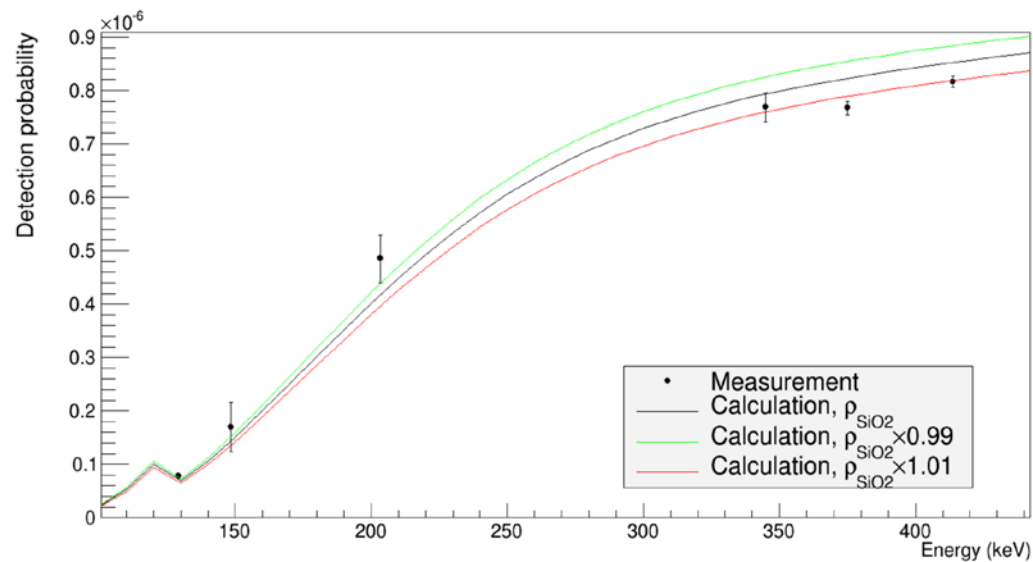
FIGURE 8 PROBABILITY OF DETECTING A PLUTONIUM GAMMA RAY EMITTED FROM THE PLUTONIUM SAMPLES AS A FUNCTION OF ENERGY, WHEN THE PLUTONIUM SAMPLES ARE PLACED AT HALF THE RADIUS OF THE DRUM AND STACKED VERTICALLY AS SHOWN IN FIGURE 7.

CHANCE

Title : Deliverable D3.3	Written:	List on Page 2	
Results of experimental investigation of calorimetry applicability	Organisation:	List on page 2	Version: 0
	Issued:	02nd April 2022	Page(s): 18
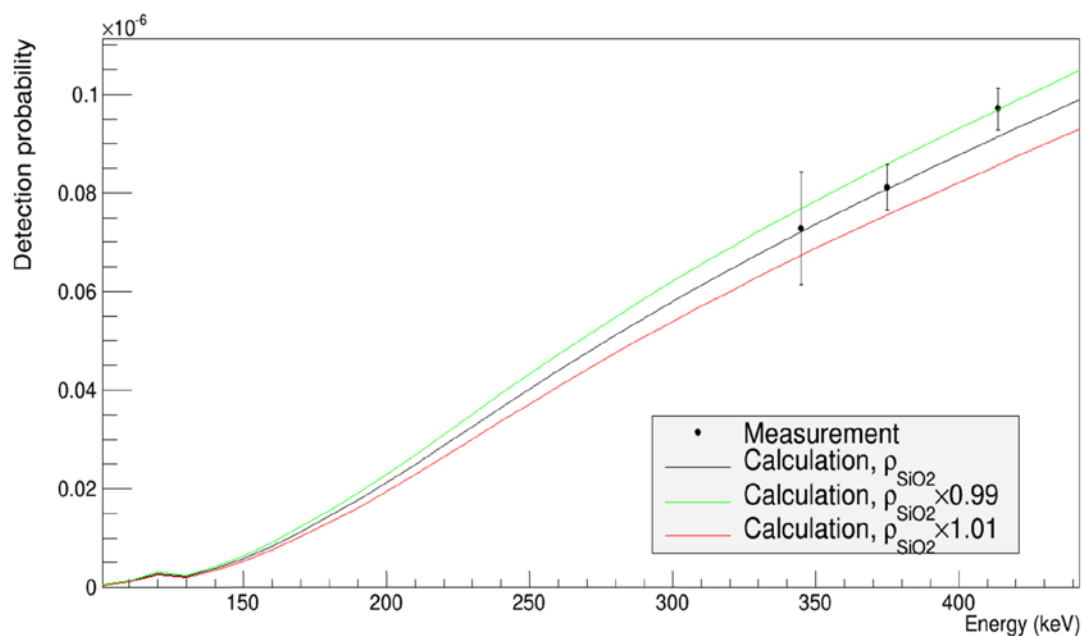
FIGURE 9 PROBABILITY OF DETECTING A PLUTONIUM GAMMA RAY EMITTED FROM THE PLUTONIUM SAMPLES AS A FUNCTION OF ENERGY, WHEN THE PLUTONIUM SAMPLES ARE PLACED IN THE MIDDLE OF THE DRUM AND STACKED VERTICALLY AS SHOWN IN FIGURE 7.
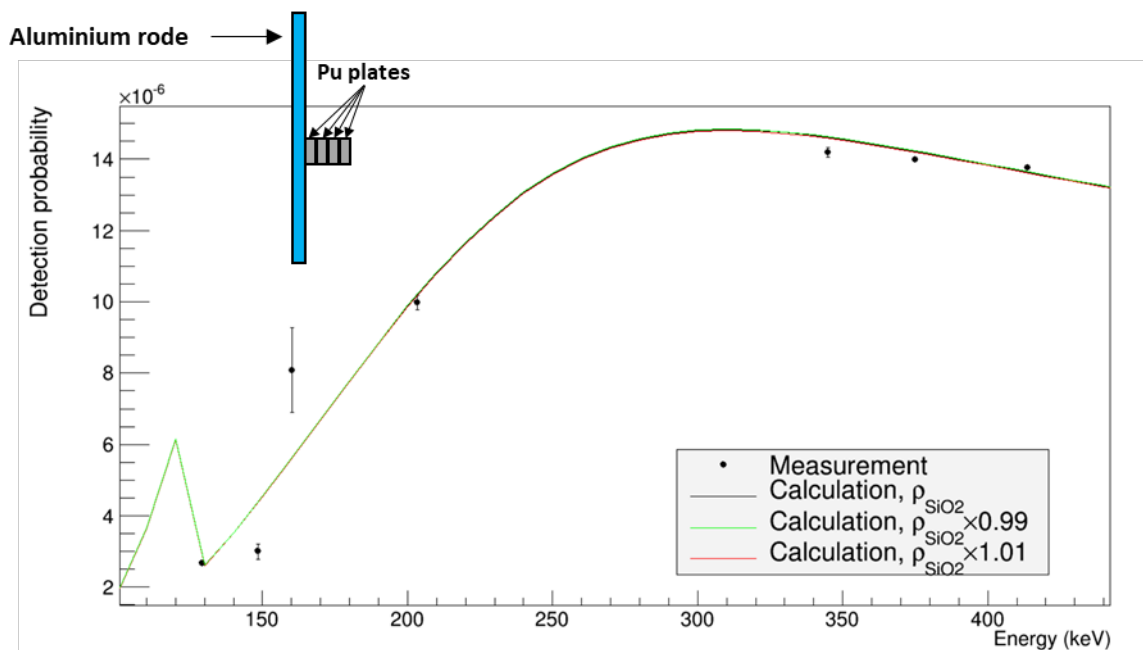
FIGURE 10 PROBABILITY OF DETECTING A PLUTONIUM GAMMA RAY EMITTED FROM THE PLUTONIUM SAMPLES AS A FUNCTION OF ENERGY, WHEN THE PLUTONIUM SAMPLES ARE PLACED IN THE PERIPHERY OF THE DRUM AND STACKED HORIZONTALLY AS SHOWN IN THE DRAWING.

3.2   Passive neutron measurement

3.2.1   Measurements

3.2.1.1   Calibration coefficient with a ^{252}Cf source

The concrete drum has been measured with the LMN transportable Passive Neutron Measurement Counting (PNMC) system shown in Figure 11. This system aims at measuring ^{240}Pu equivalent mass by measuring the rate of passive neutron coincidences in 200 L drums using ^{3}He counters surrounded by thermalizing blocs of polyethylene. This relocatable system is routinely used to inspect 200 L drums produced from an historical Cadarache radioactive waste storage area and was used in the DANAIDES facility to perform the PNM measurements for CHANCE.

CHANCE	**Title :** Deliverable D3.3	Written:	List on Page 2		
	Results of experimental investigation of calorimetry applicability	Organisation:	List on page 2	Version:	0
		Issued:	02nd April 2022	Page(s):	20
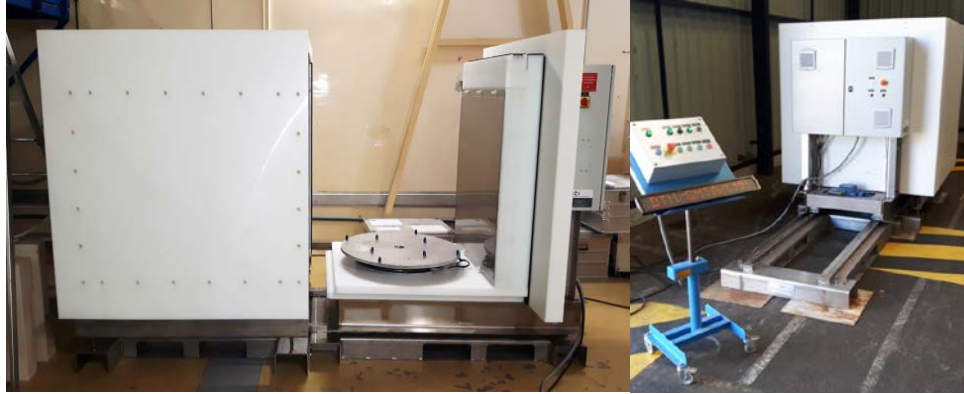
FIGURE 11 TRANSPORTABLE PASSIVE NEUTRON MEASUREMENT SYSTEM DEVELOPED BY THE NUCLEAR MEASUREMENT LABORATORY AT CEA CADARACHE.

Such a system allows measuring an equivalent ^{240}Pu mass from the measured neutron coincidence count rate through the relation:

$$m_{^{240}Pu} = \frac{R}{CC} \tag{3.2}$$

With R the neutron coincidence count rate, $m_{^{240}Pu}$ the plutonium equivalent mass and CC the Calibration Coefficient of the system.

The CC associated to the drum is measured using neutrons produced by the Spontaneous Fission (SF) of a ^{252}Cf source placed at different positions within the holes shown in Figure 5 and is estimated using:

$$k = \frac{R_{^{252}Cf}}{\frac{En_{^{252}Cf}}{\overline{v_{^{252}Cf}} \cdot \left(\overline{\frac{v(v-1)}{2}}\right)_{^{252}Cf}}} \cdot \frac{En_{^{240}Pu}}{\overline{v_{^{240}Pu}}} \cdot \left(\overline{\frac{v(v-1)}{2}}\right)_{^{240}Pu} \tag{3.3}$$

With $R_{^{252}Cf}$ the neutron coincidence rate measured with the ^{252}Cf source, En_X the neutron emission of nucleus X by Spontaneous Fission (SF), $\overline{v_X}$ the average number of neutrons emitted after a SF of X, $\left(\overline{\frac{v(v-1)}{2}}\right)_{Cf}$ the average pairs of neutrons emitted after a SF of X, with $X = {}^{252}Cf$ or $X = {}^{240}Pu$. The values of the parameters involved in eq. (3.3) are indicated in Table 1.

CHANCE

Title : Deliverable D3.3

Results of experimental investigation of calorimetry applicability

Written:	List on Page 2		
Organisation:	List on page 2	Version:	0
Issued:	02nd April 2022	Page(s):	21

TABLE 1 VALUES OF THE PARAMETERS INVOLVED IN THE EQUACTION 3.3

$En_{252_{Cf}}$	45184 s^{-1}
$En_{240_{Pu}}$	1020 s$^{-1}\cdot$ g^{-1}
$\overline{v_{252_{Cf}}}$	3.757
$\overline{v_{240_{Pu}}}$	2.156
$\overline{\left(\dfrac{v(v-1)}{2}\right)}_{252_{Cf}}$	5.981
$\overline{\left(\dfrac{v(v-1)}{2}\right)}_{240_{Pu}}$	1.913

The CC evaluated when placing the ^{252}Cf source at the positions shown in Figure 12 are presented in Table 2. The large density of the concrete matrix induces large neutron attenuation, which makes the CC very sensitive to the SF source position. There is indeed a factor of about 18 between the most sensitive area in the outskirt of the drum and the less sensitive area in the middle of the drum, making the use of PNMC very imprecise with such matrices.

CHANCE

Title : Deliverable D3.3	Written:	List on Page 2		
Results of experimental investigation of calorimetry applicability	Organisation:	List on page 2	Version:	0
	Issued:	02nd April 2022	Page(s):	22
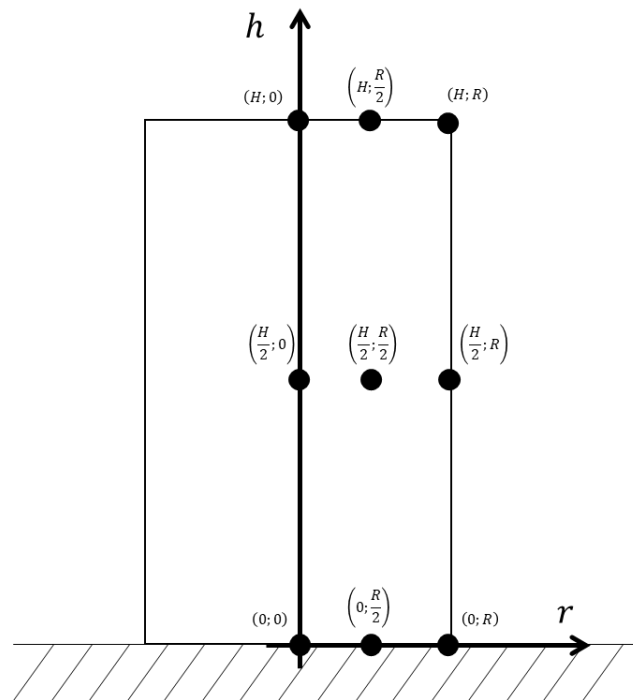
FIGURE 12 MEASUREMENT POSITIONS FOR THE PNMC MEASUREMENTS, H BEING THE DRUM HEIGH AND R BEING THE DRUM RADIUS.

TABLE 2 CALIBRATION COEFFICIENTS K MEASURED WITH A ^{252}CF SOURCE FOR THE RADIAL AND AXIAL POSITIONS SHOWN IN FIGURE 12.

r / h	0	$R/2$	R
H	1.11	1.71	4.74
$H/2$	0.81	1.60	8.99
0	0.51	0.95	5.65

3.2.1.2 Coincidence measurement of a plutonium sample

A plutonium sample has been placed at positions $\left(\frac{H}{2};0\right)$, $\left(\frac{H}{2};R\right)$, $(H;0)$, $\left(H;\frac{R}{2}\right)$ and $(H;R)$ shown in Figure 12 for which the coincidence count rate has been measured. Table 3 shows the ratio of the ^{240}Pu equivalent mass over the expected ^{240}Pu mass. The ^{240}Pu mass is estimated using the CC obtained with the ^{252}Cf source, when the ^{252}Cf was placed at the same position as the plutonium sample.

In the inner positions ($r = 0$), the measurements agree within 2 sigma with the expected mass value but for the outer positions ($r = R$ /2 and $r = R$), the difference cannot be explained by statistical uncertainties only. There are uncertainties in the isotopic composition of the plutonium sample, but they are below the observed biases.

Ideally, one should obtain the same ratio for all positions, which is not the case. Instead, the plutonium mass seems to be overestimated in the peripheral region, which indicates a bias of the measured CC versus the radius. These observations tell us that with this system and with the used concrete drum, one can expect an overall uncertainty on the ^{240}Pu mass of about 10% (or equivalently an uncertainty on the CC of about 10%).

TABLE 3 RATIO OF THE MEASURED ^{240}PU EQUIVALENT MASS OVER THE EXPECTED ^{240}PU EQUIVALENT MASS. THE UNCERTAINTY REPRESENTS STATISTICAL UNCERTAINTIES.

r \ h	0	$R/2$	R
H	1.06±0.03		1.11±0.01
$H/2$	1.08±0.04	1.13±0.03	1.10±0.01

3.2.2 Associated numerical studies

Concrete chemical composition being unknown, MCNP [6] calculations have been performed using a standard concrete composition given by Table 4 from [7]. A MCNP calculation corresponding to a homogeneous distribution leads to a calculated CC equal to 3.34 s^{-1}.g^{-1}. The measured CC cannot be measured, but can be estimated using the measurements shown in Table 2.

Indeed, one can interpolate the measurements with a function such as:

$$CC(r,h)_0 = \sum_{i=0}^{2} \left(a_i + b_i \cdot e^{c_i \cdot r/R} \right) \cdot \left(\frac{h}{H} \right)^i \tag{3.4}$$

From the $CC(r,h)$ above defined, one can estimate the CC corresponding to a homogeneous distribution $\overline{CC}_0$ averaging over the whole drum volume:

$$\overline{CC}_0 = \frac{1}{\pi R^2 H} \int_{h=0}^{H} \int_{r=0}^{R} CC(r,h)_0 \cdot 2\pi \cdot r \cdot dr dh \tag{3.5}$$

Which leads to

$$\overline{CC}_0 = \sum_{i=0}^{2} \frac{a_i}{i+1} + 2 \sum_{i=0}^{2} \frac{b_i}{i+1} \cdot \left(\frac{e^{c_i}}{c_i} \cdot \left(1 - \frac{1}{c_i} \right) + \frac{1}{c_i^2} \right) \tag{3.6}$$

Given the coefficients given in Table 5, one gets $\overline{CC_0}$=3.21.

The analytical form $CC(r,h)_0$ has the advantage to partially take into account the exponential behaviour related to neutron attenuation relative to the radius as shown in Figure 13. Let's note that an exponential fit should also be used to describe exponential attenuation along the drum high. Such a fit cannot be done since it would require additional measurements at $h = H/4$ and $h = 3H/4$ (these points would be placed before and after the maximum attenuation obtained for $h = H/2$)

Other approaches can be used, such as the polynomial fit approach described in [8]. However, with such a small number of points, the polynomial approach is not representative of reality, since, as can be seen in Figure 14, the lowest value of the fit is not necessarily at the drum centre, as one could expect since the drum is rotating. Even worst: if the attenuation is important, the polynomial fit could give rise to zones where CC is negative.

The measurement system having a small down/up asymmetry, it is expected that the maximum of attenuation is reached for a position slightly shifted relative to the mid-high of the drum, which can be seen in Figure 13 with the different CC measured for $h = 0$ and $h = H$. Contrary to radial positions, this asymmetry validates the use of a polynomial to fit axial measurements. The approach using the [8] approach nevertheless leads to a homogeneous CC $\overline{CC_1}$= 3.47 $s^{-1}. g^{-1}$.

Averaging the homogenous CC obtained using the two approaches, assuming that the true CC is bounded by $\overline{CC_0}$ and $\overline{CC_1}$, one gets $\overline{CC}$= (3.34±0.08) $s^{-1}.g^{-1}$, which is compatible with the numerical estimation obtained with MCNP using the standard concrete composition (3,34 $s^{-1}·g^{-1}$).

TABLE 4 CONCRETE COMPOSITION USED FOR THE CALCULATION OF THE CALIBRATION COEFFICIENT CC WITH MCNP.

	mass fraction (%)
H	1.00
C	0.10
O	52.91
Na	1.60
Mg	0.20
Al	3.39
Si	33.70
K	1.30
Ca	4.40
Fe	1.40
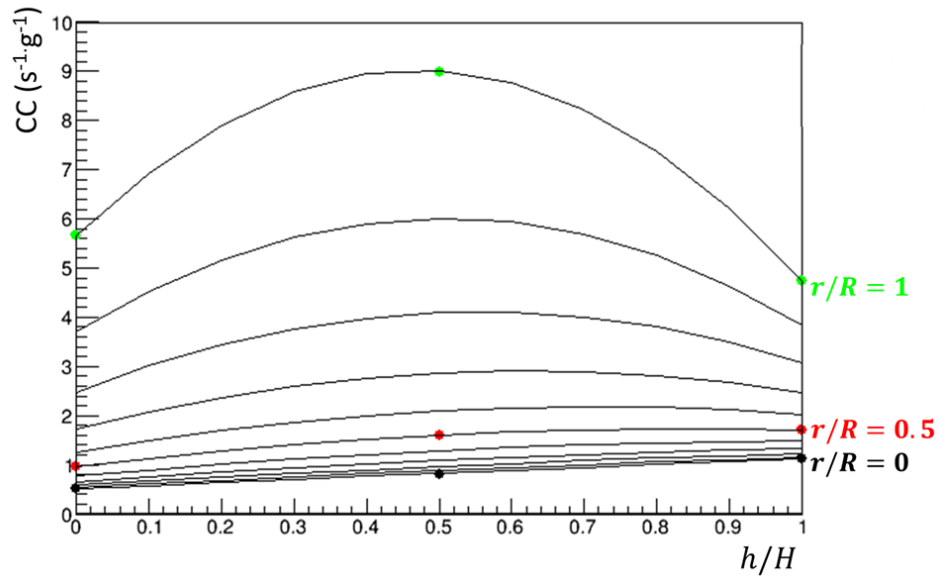
FIGURE 13 MEASURED CALIBRATION COEFFICIENTS (CC) AS A FUNCTION OF THE RELATIVE SOURCE HIGH h/H AND RELATIVE RADIUS r/R (POINTS) AND FUNCTION $CC(r,h)_0$ (LINES).
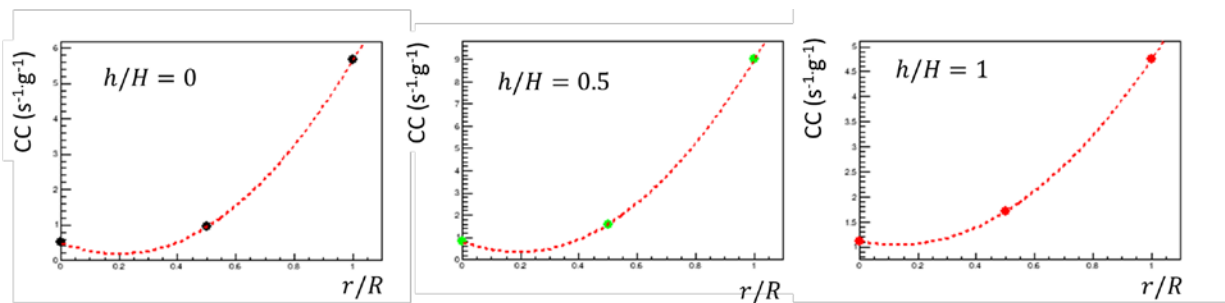
FIGURE 14 POLYNOMIAL FIT OF THE CALIBRATION COEFFICIENT AS A FUNCTION OF THE RELATIVE RADIAL POSITION WITH A SECOND DEGREE POLYNOMIAL (DASHED LINES) FOR THE THREE MEASUREMENTS POSITIONS ALONG THE DRUM AXIS.

TABLE 5 COEFFICIENTS USED TO ESTIMATE THE EXPERIMENTAL HOMOGENEOUS CC $\overline{CC}_0$.

	a_i	b_i	c_i
$i = 0$	0.464289	0.045526	4.735406
$i = 1$	0.577437	0.115789	4.778213
$i = 2$	-0.019131	-0.073884	5.328809

CHANCE

Title : Deliverable D3.3	Written:	List on Page 2		
Results of experimental investigation of calorimetry applicability	Organisation:	List on page 2	Version:	0
	Issued:	02nd April 2022	Page(s):	26

4   Calorimetric measurements at CEA

4.1   Installation of the Calorimeter

In November 2019, the calorimeter was conveyed by truck from Caluire to Cadarache and placed in the CEA DANAIDE facility which undergone modifications to enable the coming of the calorimeter. The modifications consisted in dismounting of an ancient measurement facility and adapting the electrical installation to fit the calorimeter requirements. Photos showing some steps of the installation the calorimeter in DANAIDES are shown in Figure 15.

FIGURE 15 UNLOADING OF THE CALORIMETER FROM THE TRANSPORTING TRUCK WITH A CRANE (LEFT, MIDDLE) AND TRANSFER OF THE CALORIMETER TO ITS POSITION IN THE DANAIDES FACILITY WITH A VEHICLE PUSHING THE CALORIMETER FROM THE BACK (RIGHT).

Once the calorimeter installed, the concrete drum was placed in the measurement facility as shown in Figure 16.

FIGURE 16 LOADING OF THE 200 L CONCRETE TEST DRUM IN THE CALORIMETER MEASUREMENT ROOM.

4.2 Measurements

Given that the room was poorly isolated from the outside, temperature variations were significant and difficult to mitigate. Thus, for each measurement, about 2 weeks were needed for the drum temperature to reach a satisfactory stability allowing meaningful measurement interpretation. In these conditions, the typical heat measurement time was about two weeks. To comply with safety rules related to the EURATOM rules, a padlock prevented opening the calorimeter by un-authorized CEA agents while the plutonium samples were placed in the drum instrumentation holes. When the drum was loaded with the plutonium samples, seals were also employed to check that not unexpected opening of the calorimeter happened during periods when no CEA agent could access the DANAIDES facility (nights and weekends).

CEA plutonium positions were foreseen to be placed at the $\left(\frac{H}{2};0\right)$ and $\left(\frac{H}{2};\frac{R}{2}\right)$ positions shown in Figure 12. Given the difficulties to maintain a correct temperature regulation due to the room temperature, some updates were performed by KEP to improve temperature regulation. When a satisfactory temperature regulation was obtained the measurement at $\left(\frac{H}{2};0\right)$ position in the concrete drum was performed. Unfortunately, measurements were stopped due to the COVID 19 confinement. Also, due to the calorimeter broke down during the first COVID 19 confinement, it was not possible to continue the experimental program with the $\left(\frac{H}{2};\frac{R}{2}\right)$ position. The measurements foreseen with the bitumen drum were also cancelled.

For the measurement $\left(\frac{H}{2};0\right)$, the reference measurement (baseline) was initially performed, before introducing the drum into the measuring chamber. The measurement was performed for about 200 hours (8 days), and the value was calculated using stabilized signal from the last 33 hours of measurement (Figure 17).
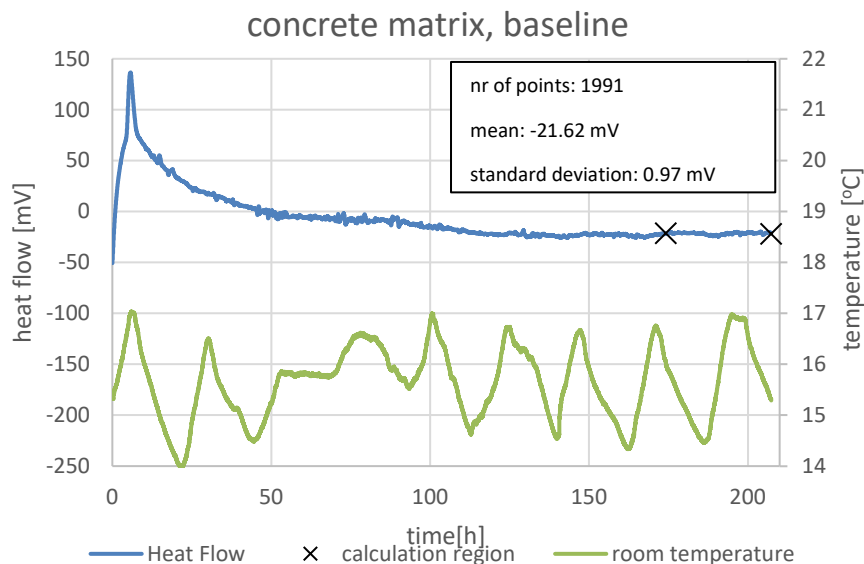
FIGURE 17. CONCRETE MATRIX, BASELINE MEASUREMENT.

The reference level stabilized at the level of about -21.62mV, with the standard deviation of 0.97mV and amplitude of temperature changes of about 1℃.

Then, the measurement was performed again with the drum that contained the Pu sample inside, placed at the $\left(\frac{H}{2}; 0\right)$ position, i.e. in the very centre of the matrix. Data were collected for about 8 days and the heat-flow determination was made using the values from the stabilized signal from the last 23 hours of measurement. The signal stabilized at the -4.73mV level with the standard deviation of 0.59mV and temperature changes with an amplitude of about 1 ° C (Figure 15).

Using the sensitivity determined during the calibration, the thermal power of the sample was calculated as the ratio of the voltage change (sample measurement minus the baseline) divided by the sensitivity:

$$P_{in} = \frac{\Delta V}{S}$$

(4.1)

Where ΔV = 16.89(1.13) mV and S =178.4(1.5) $\mu V/mW$. Then:

$$P_{in}\left(\frac{H}{2}; 0\right) = (99.7 \pm 16.4)\text{mW}$$

(4.2)

The presented uncertainty value is the uncertainty extended by the coefficient *k = 2* and corresponds to two standard deviations.
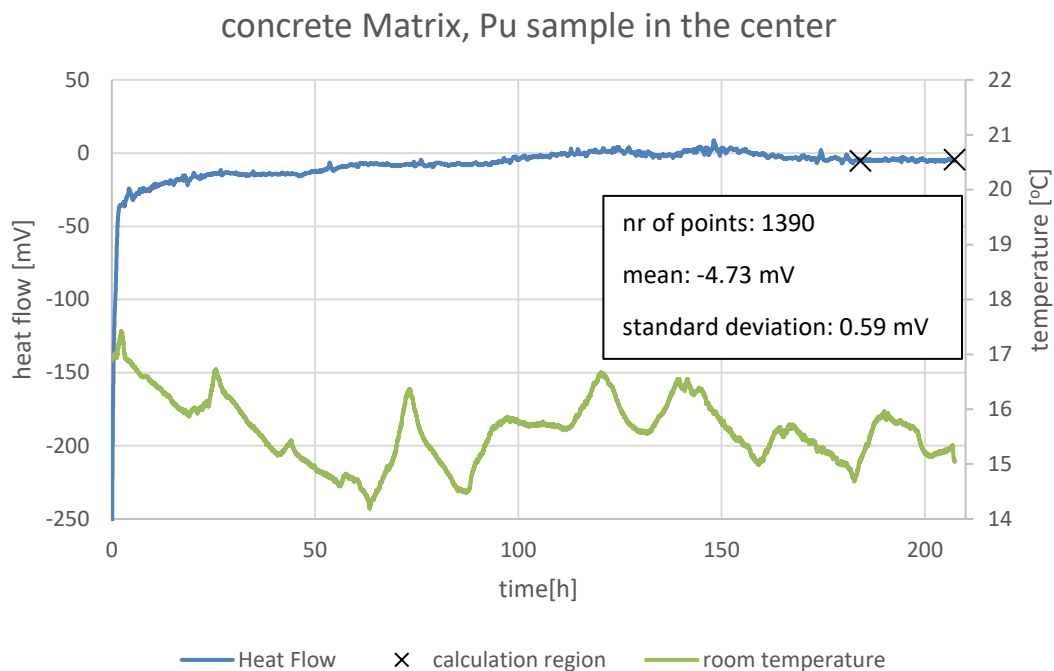
FIGURE 18. CONCRETE MATRIX, PU SAMPLE IN THE CENTRE, CALORIMETRIC MEASUREMENT.

4.3   Associated numerical studies

Energy deposition simulations were performed for the Pu of the source located at $\left(\frac{H}{2};0\right)$ position according to the real measurement. Calculations showed that for this case the gamma radiation carries only around 0.03% of the total energy, so more than 99.9% of the energy produced is deposited in the drum and wall of the drum and thus potentially can be detected by the calorimeter. The energy deposition for the sample used, determined by Monte Carlo simulation (code MCNP), corresponded to a thermal power of 106 mW. Thus, the expected value is in line with the measurement within the uncertainty range of the measured 99.7 mW, with an experimental uncertainty being 16.4 mW.

5 Non-destructive measurements at SCK CEN

5.1 Considered setups

The measurement campaign at SCK CEN was focused around three targets:

1. A measurement of a real waste drum,
2. Exploration of the effect of the spatial distribution of radioactive sources with mock-up drums/reference sources,
3. Exploration of the effect of matrix composition and density with mock-up drums/reference sources.

Both targets 2 and 3 were aimed at demonstrating the theoretical insensitivity, or robustness if you want, of the calorimeter measurement with respect to these parameters, while the efficiencies of more conventional NDA measurements are clearly influenced by them.

The corresponding list of setups, that was finally investigated with both the NDA and calorimeter measurements, is provided in Table 6.

TABLE 6. OVERVIEW OF THE DIFFERENT DRUM AND SOURCE SETUPS CONSIDERED FOR THE MEASUREMENTS AT SCK CEN.

Setup nr.	Description
Setup 1	Real unconditioned waste drum
Setup 2	7 pins (21 sources) inside mock-up 206 (mortar, extruded polystyrene (XPS))
Setup 3	1 pin (single source) in the center of mock-up 206
Setup 4	1 pin (single source) at the border of mock-up 206
Setup 5	7 pins (21 sources) inside mock-up 201 (Ethafoam)
Setup 6	7 pins (21 sources) inside mock-up 205 (Ethafoam, PVC, steel)

5.1.1 The real unconditioned waste drum

A real unconditioned waste drum (Setup 1) was selected for the real drum measurement, and only a single setup was investigated (for measurements without rotary table, one could for instance think about repeating measurements for different angles). The drum contains waste originating from the decommissioning of a MOX (Mixed Oxide Fuel) glove box, with metals as carbon steel and lead, and additionally some halogen-containing materials mixed with non-combustible waste. For efficiency calculations for this drum, the matrix was assumed to have fixed composition and density. The considered isotopic vector consists of the different Pu isotopes, Am-241, Np-237, Cm-244 and U-235. More details on the drum can be found in [26].

5.1.2 The mock-up drums and reference sources

For the mock-up drums and reference sources, we targeted three setups for exploring the effect of the spatial distribution of radioactive sources within a drum, and three setups for exploring the effect of the drum matrix, where a single setup was re-used in both cases. For the spatial distribution of sources, the same drum was used, once with 21 sources (Setup 2), and twice with a single source, one time in central position (Setup 3), and one time

near the border of the drum (Setup 4). For the effect of the matrix, the 21 sources were inserted in all three drums. More details on the mock-up drums and reference sources are provided below.

5.1.2.1   The ESARDA mock-up drums

The European Safeguards Research and Development Association (ESARDA) constructed a set of 16 so-called reference waste drums (also called ESARDA drums) [17]. Due to the high-level of design information and certification the ESARDA drums were conceived for intercomparison exercises and calibration of NDA equipment devoted to the characterization of plutonium-bearing waste drums.

Three ESARDA drums with the following filling materials were selected for the measurements within the CHANCE project:

- ESARDA drum 201: homogeneous filling with Ethafoam (polyethylene foam)
- ESARDA drum 205: heterogeneous filling with Ethafoam, PVC, and steel
- ESARDA drum 206: central section with extruded polystyrene and outer layer of mortar

ESARDA drums 201 and 205 were used in their original state, while drum 206 was modified according to the characteristics mentioned above. A central section with extruded polystyrene with a density of 37 kg/m^3 was added to ESARDA drum 206 to limit its total weight to about 300 kg.

The ESARDA drums were designed with 7 vertical channels where sources can be inserted. A schematic representation of these channels is shown in Figure 19.
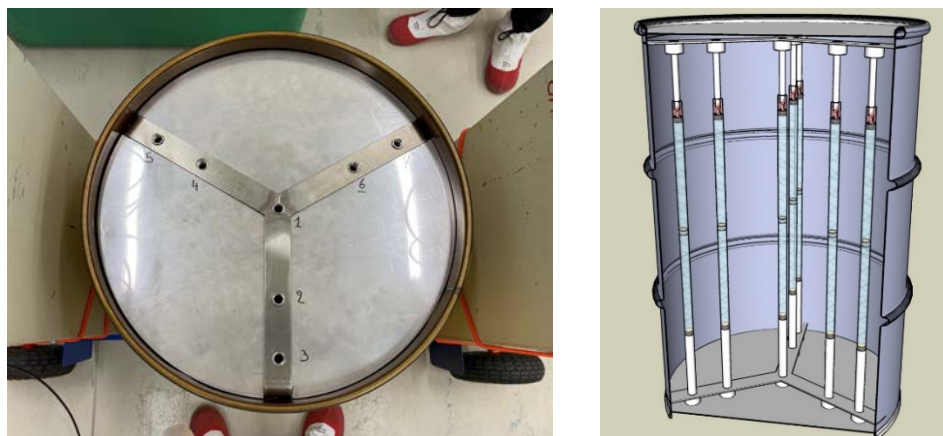
FIGURE 19. TOP VIEW OF AN ESARDA DRUM (LEFT) SHOWING THE LOCATIONS OF THE VERTICAL CHANNELS FOR THE POSITIONING OF RADIOACTIVE SOURCES, AND 3D MODEL OF THE DRUMS WITH TRANSPARENT MATRIX (RIGHT), TO VISUALIZE THE LOCATIONS OF PINS WITH SOURCES.

5.1.2.2   The ESARDA sources

Two sets of PuO$_2$ sources [18] were used during the CHANCE measurements:

CHANCE - Dissemination level: PU - Date of issue of this report: **04/04/2022** © CHANCE

This document has been produced under Grant Agreement H2020-755371. This document and its contents remain the property of the beneficiaries of the CHANCE Consortium and may not be distributed or reproduced without the express written approval of the CHANCE Coordinator.

- A first set of 1 pin with approximately 10.05 g PuO_2 in a single point, at central height of the pin (and drum),
- A second set, with 7 pins, each with approximately 1.5 g PuO_2 distributed over three axial points (top, centre and bottom of the pin), resulting in 21-point sources.

The reference mass fractions for different radionuclides of the Pu sources is included in Table 7 [19]. Given the structure of the ESARDA drums the pin with ~10.05 g of PuO_2 was placed in several positions to assess the sensitivity of the measurement technique to the source location. The second set of Pu sources was used to simulate the condition of a distributed source throughout the drum volume.

TABLE 7. ISOTOPIC COMPOSITION OF THE PU SOURCES (REFERENCE DATE: END OF 1996).

Pu isotope	Mass fraction
^{238}Pu	1.32%
^{239}Pu	64.45%
^{240}Pu	23.83%
^{241}Pu	5.75%
^{242}Pu	4.60%
^{241}Am	4.10%

5.2   Q2 and 3AX gamma spectrometry

5.2.1   Measurements

The purpose of gamma spectrometry is to identify and quantify the gamma-emitters present in the radioactive waste package by performing qualitative and quantitative analysis of the gamma spectra [9]. The mock-up drum measurements have been performed using the Q2 LLW assay system[1] displayed in Figure 20, which is a completely shielded gamma assay system.

The measurement method consists of simultaneously recording gamma spectra (59 keV to 1408 keV) on the 220-L drums with three non-collimated, high-purity germanium detectors, which are mounted through three holes in the right-side wall of the shielding cabinet one above the other. The detectors view the 220-L drum from the side at respectively the top, the mid height, and the bottom position. There is no form of collimation, so each detector crystal sees the entire interior space of the shielded measurement cabinet. The shielding cabinet is made of a 15 cm thick steel and has a hinged door to access the interior of the shielding. The inside of the cabinet is covered with a stainless-steel cladding for easy decontamination. The door is equipped with a turntable for 220 L drums which have a maximum load of 450 kg. During the measurement, the 220-L drum rotates at 10 rpm while the three detectors are used simultaneously to scan the drum. In addition, the turntable has a load cell which is connected to a weighing unit installed on top of the cabinet. The weighing unit is read out by the data acquisition PC. The chosen measurement times are 3600 s for the cases with the set of 7 pins, 21 sources, and 7200 s for those with the single pin, single source.

---

[1] https://www.canberra.com/fr/produits/waste_safeguard_systems/gamma-waste-systems.html

The data acquisition results in a spectrum per detector. These are typically merged together at the end of the measurement to form a summed spectrum, on which the remaining analysis is performed using:

- GENIE2K (Basic Spectroscopy Software [11]),
- Optional programs like Gamma Analysis Software, Interactive Peak Fit and Quality Assurance Software,

by Canberra. The GENIE2K Software makes use of an efficiency curve to determine the activities of the radionuclides. In our measurement lab, 4 standard efficiency curves are available, each associated with a specific density: 0.029, 0.411, 0.705 and 1.789 g/cm^3. An interpolation is performed between the 4 efficiency curves to calculate a specific efficiency curve for each drum, for the measurement interpretation in this document.

Setups 2 to 6 have all been measured using this Q2 system, and additionally the single source pin was also measured in position 6, in between the positions of Setup 3 (center) and Setup 4 (border).

FIGURE 20. THE Q2 LLW GAMMA ASSAY SYSTEM.

A different system, the so-called 3AX [9], was used for the real unconditioned waste drum (Setup 1) segmented gamma scanning, as detailed in [26], because of a too high dose rate of the drum (> 20 μSv/h). The 3AX is a SGS device, which scans in the horizontal plane while the drum is rotating. Here, we only used the rotation capability and varied the height of the 3AX detector along the vertical axis of the drum. A 3AX SGS is made of three parts: the mechanics, the detector system and the data acquisition and processing unit. The mechanical system consists of an evaluation unit for the turntable and two trolleys positioned respectively on the left- and right-hand side of the turntable opposite to one another. The right trolley holds the detector–collimator system while the left one can be equipped with a transmission source (which has not been used here). Both trolleys can move horizontally towards and from the drum. The SGS is equipped with a high purity germanium detector (HPGe) connected to a cooling unit using liquid nitrogen. This detector is fixed in a lead collimator, enabling it to ''see'' only a fraction of the waste package. The slice of a drum that can be seen by the detector is defined by the aperture of the collimator and the distance between detector and waste package. The measurement setup details are as follows:

- The detector is surrounded by a rectangular lead slit collimator with a 1 mm copper coating (5◦ opening; 18 mm × 110 mm; 100 mm depth).

- The 220-L drum is placed on a turning table and is continuously rotated during the measurements, with a rotation rate of 10 rotations per minute.
- The drum is discretized into 20 horizontal segments resulting in 20 individual spectra.
- Measurement time per segment is 300 s.

Data acquisition is performed and controlled by the main program which communicates with the Genie-2000 [11] software for conventional activity estimation. Here the scans of 20 segments were not combined but used individually, in order to retrieve some information on the distribution of activities along the vertical axis of the drum.

To account for the effect of the uncertainty associated with the (unknown) source distribution within the drum on the detector efficiencies, the whole measurement system is modelled using the complex cylinder model of the Geometry Composer V4.3 library of the ISOCS/LabSOCS software [10]. Drum dimensions, filling degree and mean matrix composition and density are kept fixed in the ISOCS model and the only parameter that is varied is the source distribution. Two extreme source distributions are modelled, a homogeneous source distribution within each segment (considered to be the maximum possible efficiency) and a point source placed on the drum axes on the border of a segment (considered to be the minimum possible efficiency).

In case of the real drum, there are no reference values, and a first interpretation is therefore not included here (but is available in [26]). The interpretation in terms of activities will only reported in the next step during the probabilistic modelling.

5.2.2 Results

The results for measuring the mock-up drums with 7 pins (Setups 2, 5 and 6) show a decrease in the count rate as the density of the measured drum increases (Table 8). Compared to Setup 5 (drum 201, Ethafoam):

- Setup 6 (drum 205, Ethafoam, PVC and steel): For the low energies, a factor of 1.5 times lower count rates was determined. This factor decreases as the gamma energy increases.
- Setup 2 (drum 206, mortar and XPS): For the low energies, a factor of 15 times lower count rates was determined. This factor drops to 5 with higher energies.

Figure 21 shows the relative deviations between the calculated activities and the reference activity for a homogeneous source distribution (7 pins) for the different drum material compositions, Setups 5, 6 and 2. Table 9 provides an overview of the estimated activities. We notice that the measured/modelled results fit relatively well for the high energy lines for Setup 5 (drum 201) and Setup 6 (drum 205). The discrepancies between calculated/measured and reference activity are bigger for Setup 2 (drum 206), because of a higher density of the matrix.

The results for measuring mock-up drum 206 with one pin on different positions (Setups 3 and 4, and the intermediate position) show for every energy line the highest count rate in the most peripheral location in Setup 4 (Table 10):

- For the very low energy lines, the count rate increases as the position of the pin moves from the centre to the periphery of the measured drum.
- For the very high energies, no spectacular differences were obtained for the count rates between the different pin positions.
- For the energy lines in between, the count rates for the intermediate position 6 are the lowest compared to positions 1 (Setup 3) and 7 (Setup 4).

CHANCE

Title : Deliverable D3.3

Results of experimental investigation of calorimetry applicability

Written:	List on Page 2		
Organisation:	List on page 2	Version:	0
Issued:	02nd April 2022	Page(s):	35

Figure 22 shows the relative deviations between the total calculated activities and the reference activity for point source distributions (1 pin) in drum 206. Table 11 provides an overview of the estimated activities. We notice that the measured/modelled results fit relatively well for the radionuclides Pu-239, Pu-240, Pu-241 and Am-241, when the pin is at position 7. The discrepancies between calculated/measured and reference activity are large for the other two positions, 1 and 6, for all radionuclides.

Note that the results presented here represent a first estimate. More detailed Monte Carlo particle transport efficiency calculations will be done later, as input to the probabilistic modelling exercise, where we will present the final interpretation of the measurements in terms of activities.

TABLE 8. COUNT RATES OBTAINED FOR THE DIFFERENT CONSIDERED GAMMA LINES FOR THE MEASUREMENTS WITH 7 PINS AND 21 SOURCES, IN EACH OF THE THREE MOCK-UP DRUMS.

Radionuclide	E(keV)	Count rate (E, R*) [s-1]		
		Setup 2 (drum 206)	Setup 5 (drum 201)	Setup 6 (drum 205)
Am-241	125,30	2,81E+04	4,06E+05	2,87E+05
Pu-239	129,29	8,52E+03	1,14E+05	8,32E+04
Pu-241	148,57	1,73E+04	2,93E+05	1,95E+05
Pu-238	152,72	9,26E+03	1,60E+05	1,05E+05
Pu-240	160,31	1,98E+03	4,27E+04	2,63E+04
Pu-241 eqU237	164,58	9,03E+03	1,36E+05	9,28E+04
Am-241	169,56	4,74E+03	6,60E+04	4,49E+04
Pu-239	203,55	5,46E+03	5,49E+04	4,04E+04
Pu-241 eqU237	208,00	2,23E+05	2,85E+06	2,04E+06
Am-241	322,52	1,42E+04	1,38E+05	1,04E+05
Pu-239	345,01	7,73E+03	7,10E+04	5,45E+04
Pu-239	413,70	2,26E+04	1,92E+05	1,48E+05
Pu-239	451,48	3,40E+03	2,64E+04	2,01E+04
Pu-239	645,90	2,61E+02	1,23E+03	9,60E+02
Am-241	662,40	4,31E+04	2,65E+05	2,15E+05
Am-241	722,01	2,35E+04	1,36E+05	1,11E+05
Pu-238	766,36	2,41E+03	1,42E+04	1,13E+04

CHANCE

Title : Deliverable D3.3

Results of experimental investigation of calorimetry applicability

Written:	List on Page 2		
Organisation:	List on page 2	Version:	0
Issued:	02nd April 2022	Page(s):	36

FIGURE 21. RELATIVE DIFFERENCES (%) IN TOTAL ACTIVITY BETWEEN THE FIRST ACTIVITY ESTIMATES AND THE REFERENCE VALUES, FOR THE MEASUREMENTS WITH 7 PINS AND 21 SOURCES, IN EACH OF THE THREE MOCK-UP DRUMS.

TABLE 9. A FIRST ESTIMATE OF ACTIVITIES FOR THE MEASUREMENTS WITH 7 PINS AND 21 SOURCES, IN EACH OF THE THREE MOCK-UP DRUMS.

Radionuclide	E(keV)	Reference Activity (Bq)	Activity (Bq) Setup 2 (206)	Average	Setup 5 (201)	Average	Setup 6 (205)	Average
Am-241	125,30	8,79E+10	2,25E+09	2,96E+09	6,86E+09	1,06E+10	5,76E+09	8,50E+09
	169,56		5,02E+09		2,19E+10		1,64E+10	
	322,52		2,29E+10		6,48E+10		5,56E+10	
	662,40		4,06E+10		7,69E+10		6,91E+10	
	722,01		4,25E+10		7,72E+10		6,97E+10	
Pu-239	129,29	1,31E+10	4,92E+08	9,90E+08	1,17E+09	1,75E+09	1,04E+09	1,50E+09
	203,55		1,92E+09		5,45E+09		4,63E+09	
	345,01		3,74E+09		9,99E+09		8,83E+09	
	413,70		4,19E+09		1,01E+10		8,84E+09	
	451,48		5,26E+09		1,17E+10		1,01E+10	
	645,90		5,99E+09		9,07E+09		9,35E+09	
Pu-241	148,57	6,49E+11	2,20E+10	2,91E+10	9,27E+10	1,74E+11	7,27E+10	1,47E+11
Pu-241	164,58		2,07E+10		1,61E+11		1,28E+11	
eqU237	208,00		8,77E+10		3,05E+11		2,53E+11	
Pu-238	152,72	6,22E+10	2,16E+09	2,68E+10	9,77E+09	7,32E+10	7,62E+09	6,36E+10
	766,36		3,99E+10		7,41E+10		6,49E+10	
Pu-240	160,31	1,78E+10	NA		5,66E+09	5,66E+09	4,08E+09	4,08E+09

TABLE 10. COUNT RATES OBTAINED FOR THE DIFFERENT CONSIDERED GAMMA LINES FOR THE MEASUREMENTS WITH A SINGLE PIN AND SOURCE, IN EACH OF THE THREE PIN POSITIONS.

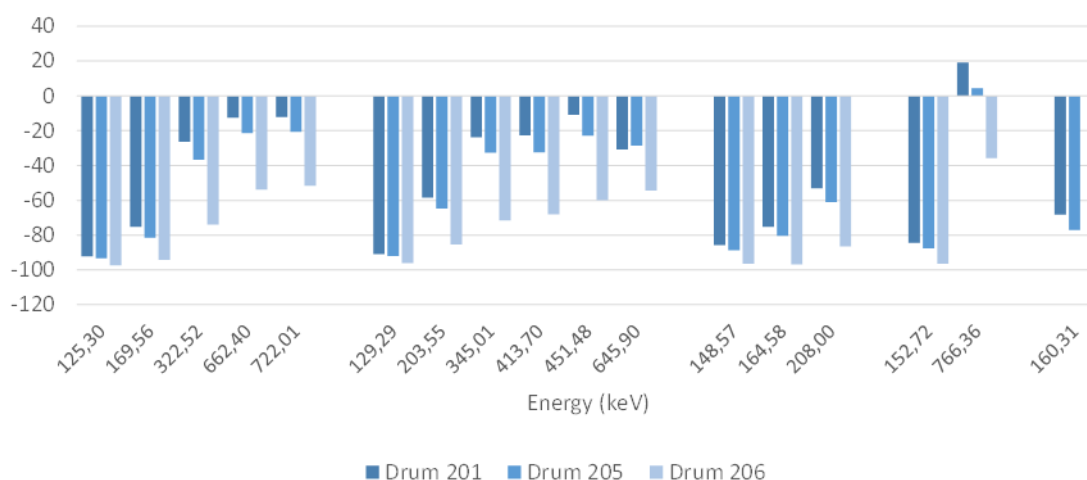| Radionuclide	E(keV)	Count rate (E, R*) [s⁻¹]		
		Setup 3 (position 1)	Extra setup (position 6)	Setup 4 (position 7)
Am-241	125,30	7,68E+03	9,18E+03	4,60E+04
Pu-239	129,29	1,54E+03	2,44E+03	1,31E+04
Pu-241	148,57	1,81E+04	1,21E+04	3,06E+04
Pu-238	152,72	9,55E+03	7,47E+03	1,71E+04
Pu-240	160,31	2,54E+03	8,46E+02	3,48E+03
Pu-241 eqU237	164,58	9,69E+03	5,81E+03	1,53E+04
Am-241	169,56	5,59E+03	3,71E+03	7,95E+03
Pu-239	203,55	7,73E+03	6,68E+03	9,04E+03
Pu-241 eqU237	208,00	2,76E+05	2,18E+05	4,06E+05
Am-241	322,52	2,33E+04	1,86E+04	2,92E+04
Pu-239	345,01	1,30E+04	1,07E+04	1,61E+04
Pu-239	413,70	4,15E+04	3,38E+04	4,78E+04
Pu-239	451,48	6,04E+03	5,10E+03	6,72E+03
Pu-239	645,90	5,35E+02	4,95E+02	3,04E+02
Am-241	662,40	8,62E+04	7,37E+04	8,89E+04
Am-241	722,01	4,74E+04	4,09E+04	4,85E+04
Pu-238	766,36	5,11E+03	4,56E+03	5,16E+03
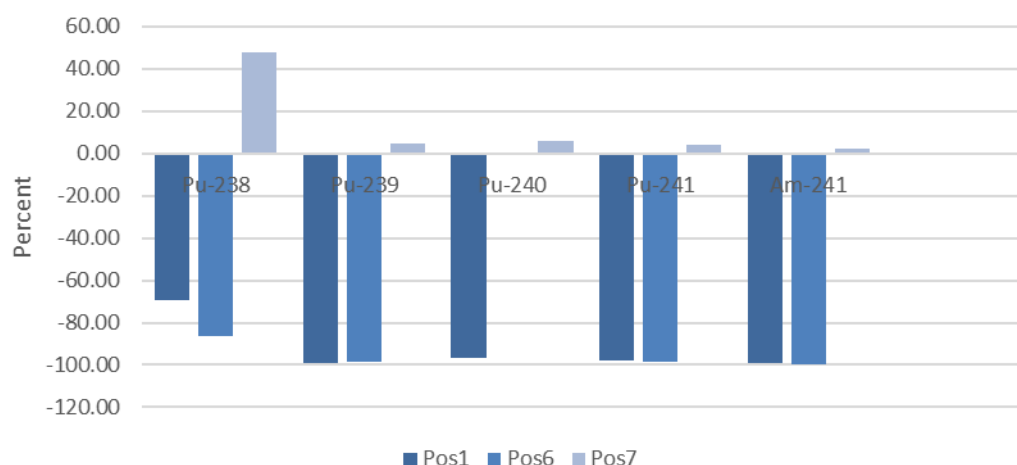
FIGURE 22. RELATIVE DIFFERENCES (%) IN TOTAL ACTIVITY BETWEEN THE FIRST ACTIVITY ESTIMATES AND THE REFERENCE VALUES, FOR THE MEASUREMENTS WITH A SINGLE PIN AND SOURCE, IN EACH OF THE THREE PIN POSITIONS.

CHANCE

Title : Deliverable D3.3

Results of experimental investigation of calorimetry applicability

Written:	List on Page 2		
Organisation:	List on page 2	Version:	0
Issued:	02nd April 2022	Page(s):	38

TABLE 11. A FIRST ESTIMATE OF ACTIVITIES FOR THE MEASUREMENTS WITH A SINGLE PIN AND SOURCE, IN EACH OF THE THREE PIN POSITIONS.

Radionuclide	E(keV)	Reference Activity (Bq)	Activity in mock-up drum 206, 1 pin (Bq)					
			Setup 3 (pos. 1)	Average	Extra set. (pos. 6)	Average	Setup 4 (pos. 7)	Average
Am-241	125,30	8,46E+10	2,45E+08	6,25E+08	2,88E+08	3,32E+08	1,64E+09	2,04E+09
	169,56		2,36E+09		2,04E+09		4,41E+09	
	322,52		1,75E+10		1,42E+10		2,41E+10	
	662,40		3,71E+10		3,17E+10		4,19E+10	
	722,01		3,90E+10		3,38E+10		4,36E+10	
Pu-239	129,29	1,26E+10	2,99E+07	8,75E+07	3,89E+07	1,72E+08	3,13E+08	5,85E+08
	203,55		1,21E+09		1,05E+09		1,65E+09	
	345,01		2,93E+09		2,31E+09		3,90E+09	
	413,70		3,61E+09		2,87E+09		4,40E+09	
	451,48		4,30E+09		3,69E+09		5,22E+09	
	645,90		5,57E+09		3,72E+09		5,46E+09	
Pu-241	148,57	6,24E+11	1,03E+10	1,39E+10	6,82E+09	9,58E+09	1,88E+10	2,66E+10
Pu-241	164,58		1,79E+10		1,30E+10		3,76E+10	
eqU237	208,00		4,98E+10		3,92E+10		8,04E+10	
Pu-238	152,72	5,98E+10	1,06E+09	1,83E+10	8,01E+08	8,28E+09	1,96E+09	2,86E+10
	766,36		3,88E+10		3,13E+10		4,26E+10	
Pu-240	160,31	1,71E+10	5,82E+08	5,82E+08	NA	NA	9,71E+08	9,71E+08

5.3 ISOCS gamma spectrometry and application of FRAM

The different setups have been characterized additionally using open geometry high-resolution gamma spectrometry with an ISOCS (In Situ Object Counting System) calibrated detector [9]. Modification of the multi-channel analyser settings allowed two types of spectral analysis:

- Conventional spectral analysis using standard Genie 2000 [11] and ISOCS software.
- Specific plutonium and uranium isotopic analysis using the FRAM (Fixed energy, Response function Analysis with Multiple efficiencies) software [12].

5.3.1 Measurements

The broad energy planar detector b015061 model BE3830P has a detector crystal with an active area of 3800 mm² and a thickness of 32 mm. The relative efficiency is typically 34% and the resolution at 122 keV is 0.720 keV. As shown in Figure 23:

- The 220-L drum (yellow) was placed on the Q2 rotating table.
- The HPGe detector was placed horizontally and pointing towards the central axis at half drum height.
- The detector crystal was shielded at the side and the back using lead. The lead collimator in front has an opening of 90°.
- The distance between the detector and the outer surface of the 200-L drum at half height was:
  - 1 meter for mock-up drums in Setups 3 to 6.
  - 4.27 meters for the real drum (Setup 1), due to the high gamma signal. In this case, measurements were performed with and without additional front shielding to reduce the signal from the 60 keV photopeak of Am-241.

- The data acquisition times ranged from about 4.5 h up to nearly 65 h.

Setup 2 (mock-up drum 206 with 7 pins and 21 sources) was not measured by gamma spectrometry ISOCS/FRAM.

FIGURE 23. OPEN GEOMETRY GAMMA SPECTROMETRY WITH ISOCS

5.3.2   Results

In order to calculate the activities of the individual radionuclides, the ISOCS software allows drafting various models for each measurement setup. In some cases, the LACE (Line Activity Consistency Evaluator) option was used to optimize the results. Additional to the activity estimates, the application of the FRAM software resulted in estimates on the Pu isotopic vector.

We do not report on the results for the real drum (Setup 1) and for mock-up 205 (Setup 6). In case of the real drum, there is no reference value and measurements for both drums were only performed for the probabilistic modelling in the next step.

5.3.2.1   Setups 3 and 4

Figure 24 shows the relative deviations between the calculated activities and the reference activity for a point source placed at half height of the drum in the central (Setup 3, position 1), intermediate (extra measurement with source at position 2, in between the positions of Setup 3 and Setup 4) and eccentric (Setup 4, position 3) positions. We notice that the measured/modelled results fit relatively well for the point source models, even when the source is placed in the intermediate position. Differences are getting larger for the point source placed in the eccentric position. Higher gamma ray-energy results in a decreasing discrepancy between calculated/measured and reference activity. Therefore, differences for Pu-238, Pu-239 and Am-241 are smaller, compared to those for Pu-240 and Pu-241.

CHANCE

Title : Deliverable D3.3

Results of experimental investigation
of calorimetry applicability

Written:	List on Page 2		
Organisation:	List on page 2	Version:	0
Issued:	02nd April 2022	Page(s):	40

FIGURE 24. RELATIVE DIFFERENCE BETWEEN THE CALCULATED ACTIVITY A, FOR THE MOST ENERGETIC GAMMA-RAY OF AN IDENTIFIED RADIONUCLIDE FOR TWO ISOCS MODELS, AND THE REFERENCE ACTIVITY, FOR SETUP 3 (POSITION 1), THE INTERMEDIATE POSITION (2) AND SETUP 4 (POSITION 3).

Figure 25 shows the relative discrepancies between the plutonium isotopic composition provided by FRAM and the reference isotopic composition for the single source placed in Pos1 and Pos2. The results using the FRAM code correspond very well with the reference values. Uncertainties are however relatively large for the mock-up 206 high-density matrix.

FIGURE 25. RELATIVE DISCREPANCIES BETWEEN THE PLUTONIUM ISOTOPIC COMPOSITION, PROVIDED BY FRAM, AND THE REFERENCE ISOTOPIC COMPOSITION FOR SETUP 3 (206 POS 1) AND THE INTERMEDIATE POSITION FOR MOCK-UP DRUM 206. THE ERROR BARS INDICATE THE ±2S UNCERTAINTIES PROVIDED BY FRAM.

5.3.2.2 Setup 5

The relative deviations between the calculated activities for the most energetic gamma ray of an identified radionuclide for various ISOCS models, and the reference activity, are reported in Figure 26. The overall best performing model "homogeneous 2", considered a fully homogeneous source and matrix distribution, taking all materials into account (not only the ethafoam matrix but as well the zircaloy source packaging and tubing system to place the sources). We notice larger differences for the "homogeneous 3" model, consisting of a fully homogeneous source distribution in an ethafoam matrix and separately accounting for the zircaloy shielding. Adjusting the zircaloy thickness in the model to obtain an optimal LACE, only improves the results for Pu-240, Pu-241 and Am-241. Increasing gamma ray energy results in decreasing discrepancy between calculated/measured and reference activity. Therefore, differences for Pu-238, Pu-239 and Am-241 are smaller, compared to those for Pu-240 and Pu-241.
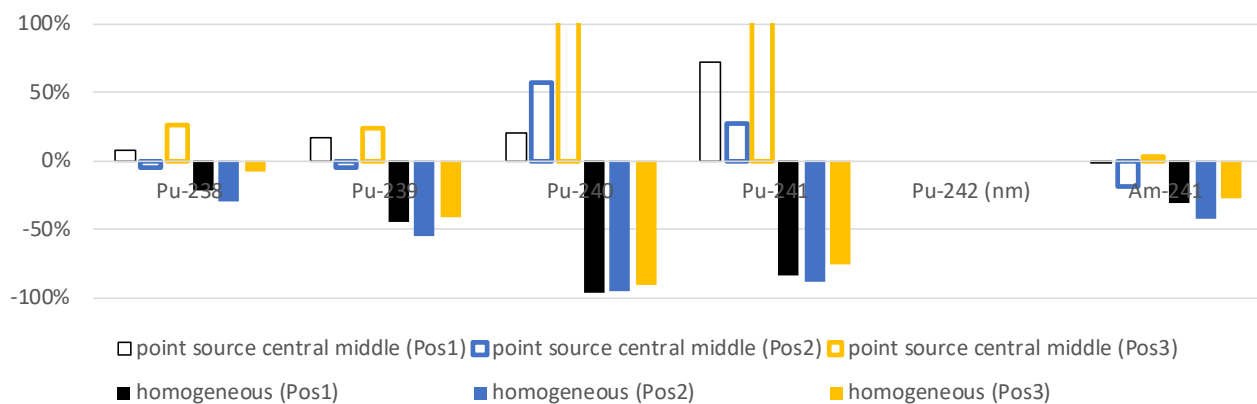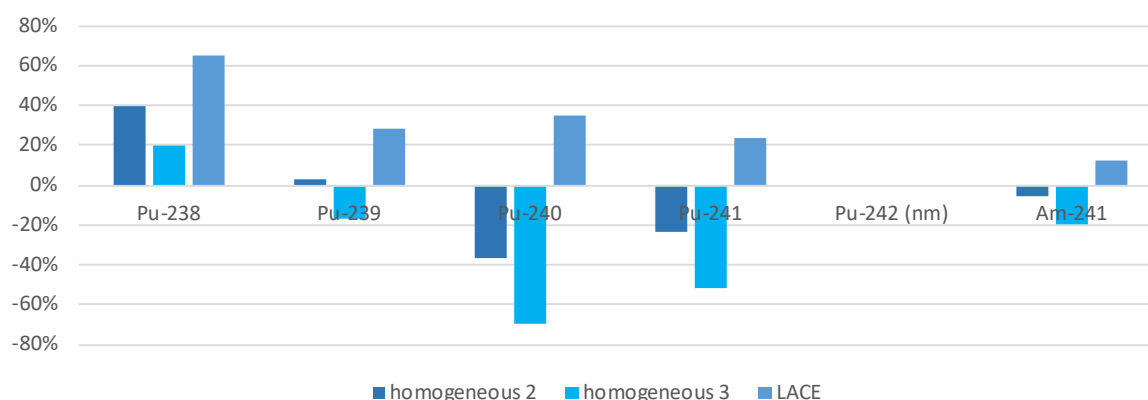

FIGURE 26. RELATIVE DIFFERENCE BETWEEN THE CALCULATED ACTIVITY A, FOR THE MOST ENERGETIC GAMMA-RAY OF AN IDENTIFIED RADIONUCLIDE FOR TWO ISOCS MODELS, AND THE REFERENCE ACTIVITY, FOR SETUP 5.

Figure 27 shows the relative discrepancies between the plutonium isotopic composition provided by FRAM and the reference isotopic composition for two types of measurement modes: the drum rotating around its axes during the measurement and the drum standing in a fixed position during the measurement. With the exception of Pu-242, the results using the FRAM code correspond « exceedingly » well with the reference values due to the lower matrix density compared to mockup drum 206 (see Figure 25).
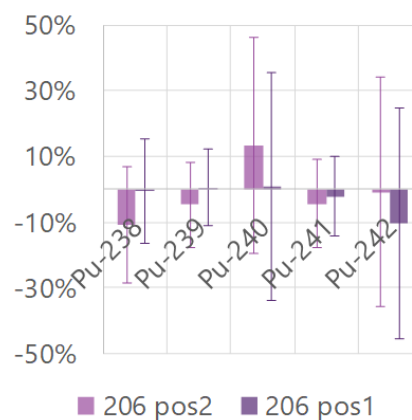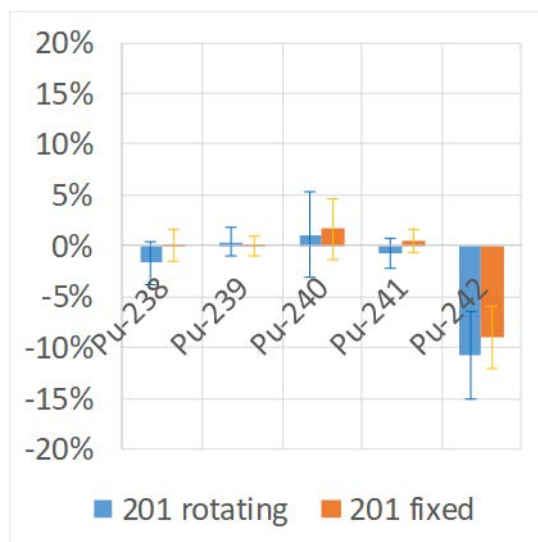
FIGURE 27. RELATIVE DISCREPANCIES BETWEEN THE PLUTONIUM ISOTOPIC COMPOSITION, PROVIDED BY FRAM, AND THE REFERENCE ISOTOPIC COMPOSITION AND TWO TYPES OF MEASUREMENTS OF SETUP 5, MOCK-UP DRUM 201 (ROTATING AND FIXED DURING THE MEASUREMENT). THE ERROR BARS INDICATE THE ±2S UNCERTAINTIES PROVIDED BY FRAM.

5.4 Passive neutron coincidence counting

5.4.1 Measurements

5.4.1.1 Slab counters and electronics

Two Canberra WM3400 slab counters [12] were used for the measurements within the CHANCE project. A picture of the detectors during the measurement of a drum is shown in Figure 28. To ensure an accurate positioning of the drum and detectors, a square metal frame was placed around the drum (see Figure 2 at the bottom of the ESARDA drum). The two slab counters were positioned in contact with the metal frame on opposite sides. By using the metal frame the distance between the slab counters was either 74 or 76 cm in two different measurement campaigns. The detectors had to be repositioned manually and the positioning of the slab counters could be reproduced with an accuracy of less than 1 cm. In addition, we verified that the distance between the detectors at the top and at the bottom varied, depending on the measurement point, within 1 cm.

FIGURE 28. PICTURE OF A MEASUREMENT WITH THE WM3400 SLAB COUNTERS AND THE ESARDA DRUM 206.

Each WM3400 counter measures 104 cm (height) $\times$ 41 cm (width) $\times$ 16 cm (depth) and has an approximate weight of 50 kg. To facilitate the movement and positioning of the WM3400 each slab counter has been fixed to a moving cart as shown in Figure 28. The WM3400 counter contains six ^{3}He tubes (active length of 91.44 cm and diameter of 2.54 cm) which are positioned in-line and embedded in a polyethylene slab. The polyethylene slab is then surrounded by 1-mm Cd sheet that covers five sides of the slab. During a measurement the WM3400 should be placed such that the side without the Cd cover is facing the sample being measured. An additional aluminium sheet covers the slab counter and provides further protection to the inner components.

The default electronic system of the WM3400 has been replaced to reduce the electronic noise and gamma-ray sensitivity [14]. The updated electronic system includes a dedicated preamp for each ^{3}He tube, the possibility to adjust for gain differences between the ^{3}He tubes, and an optimised shaping time for ^{3}He detectors. During the CHANCE measurements two types of data acquisition systems were used in parallel. First a system based on JSR-12 shift registers [15] was used. One JSR-12 shift register was connected to each slab counter, and one JSR-12 was used to process the logical OR of the signals coming from both slab counters. In addition, the time stamps of the neutron detections were recorded with the MCA-527 multi-channel analyser equipped with time stamp processing firmware [16]. The shift registers recorded the measurement time t, the Total events T, Real+Accidental events $R+A$, and Accidental events A. The time stamps recorded by the MCA-527 were further processed off-line with a dedicated software to determine T, $R+A$, and A events, the multiplicity distribution, as well as to remove system instabilities due to high voltage and fluctuations or interferences.

In addition to the ESARDA sources, a ^{252}Cf source with a nominal activity of 37kBq on 15 August 2015 was used also as calibration source. The ^{252}Cf source was used in the standard measurement setup without the presence of a drum, or inserted in one of the ESARDA drums.

5.4.1.2   Considered measurements

The list of measurements carried out with the slab counters within the CHANCE project is summarized in Table 12. The measurement campaign took place in two periods, March 2020 and March 2021, due to an interruption related

CHANCE

Title : Deliverable D3.3

Results of experimental investigation of calorimetry applicability

Written:	List on Page 2		
Organisation:	List on page 2	Version:	0
Issued:	02nd April 2022	Page(s):	44

to the Covid-19 outbreak. For the first two measurements in Table 12, no drum was present in the room and the sources (when present) were placed between the detectors. Equal distancing between source and detector was ensured with the metal frame shown in Figure 28.

The measurements with the ESARDA drum 201 consisted in a background measurement with only the drum placed between the detectors, measurements with the ^{252}Cf source or the single pin single source placed in different positions within the drum, and measurement with the 7 pins, 21 sources placed in all available positions (Setup 5). A similar series of measurements was conducted with the ESARDA drum 206, but in this case a total of 7 measurements were carried out with the single pin, single source, considering all measurement positions except for position 4 (i.e. including Setups 2, 3 and 4). The measurement in position 3 was carried out twice to assess the repeatability of the measurement approach. The measurements with the ESARDA drum 205 consisted in the measurement of background, ^{252}Cf source, and the 7 pins, 21 sources (Setup 6).

TABLE 12. BACKGROUND SUBTRACTED TOTALS AND REALS RATE VALUES FOR THE MEASURED COMBINATIONS OF DRUMS AND SOURCES AT DIFFERENT POSITIONS. THE UNCERTAINTY ON THE TOTALS RATE WAS ALWAYS AT MOST 0.1 S-1.

Drum	SOURCE	Position	Setup	T_{exp} / s^{-1}	$R_{exp,m}$ / s^{-1}
None	^{252}**Cf**	**1**		27.1	0.77(<0.01)
	1 pin	**1**		242.3	1.75(0.01)
201	^{252}**Cf**	**1**		29.8	0.76(<0.01)
		3		25.9	0.43(<0.01)
		7		47.7	1.58(0.01)
	1 pin	**1**		262.3	1.54(0.01)
		2		226.7	1.12(0.01)
		3		176.4	0.67(0.01)
		5		333.0	2.72(0.02)
		7		320.8	2.54(0.02)
	7 pins	**All**	**Setup 5**	260.5	1.53(0.01)
205	^{252}**Cf**	**1**		26.0	0.64(<0.01)
	7 pins	**All**	**Setup 6**	239.7	1.39(0.01)
206	^{252}**Cf**	**1**		24.5	0.50(<0.01)
		7		35.1	1.07(0.01)
	1 pin	**1**	**Setup 3**	218.9	0.99(0.01)
		2		182.0	0.66(0.01)
		3		91.1	0.14(>0.01)
		3		90.9	0.14(<0.01)
		5		240.8	1.19(0.01)
		6		341.6	2.66(0.02)
		7	**Setup 4**	358.8	2.93(0.02)
	7 pins	**All**	**Setup 2**	222.6	1.08(0.01)

The measurement data from the time stamps recorded with the MCA527 were analysed by means of Python [20] scripts, in the Spyder environment version 4 [21]. The scripts first carried out stability checks of the data by monitoring the total count rate over a 10 second interval. Then the data were analysed to determine the totals and the reals rate for each measurement. The background subtraction was then carried out and the net total and net real count rates, indicated with T_{exp} and $R_{exp,m}$, respectively, in Table 12, were determined.

The obtained data were used to determine the mass of the assayed sample by applying two methodologies, one based on the point model approximation, and one based on Monte Carlo modelling.

5.4.2   Data analysis

5.4.2.1   Point model approach

Starting from basic principles, theories were developed [22], [23], [24] that express the observables of neutron coincidence or multiplicity measurement as function of the mass of neutron emitting radionuclides and other parameters. This model, called the point model, can be applied in case the assayed sample has point geometry, no neutrons return from the detector to the sample, the time response function of the moderator detector assembly is a pure exponential function with decay constant, and there are no dead time losses of signals. Other conditions additionally apply, but we refer to the references for the full description.

In absence of multiplication, the theoretical estimates from the point model of Hage [24] are the following for the totals and reals rate:

$$T_{pm} = \varepsilon F_s M v_{s(1)}[1 + \alpha] \qquad (5.1)$$

$$R_{pm} = \varepsilon^2 F_s M^2 v_{s(2)} \qquad (5.2)$$

Where

- ε is the (total) detection efficiency

- F_s the spontaneous fission rate of the test item

- $\alpha = \frac{F_s}{S_\alpha}$

- S_α the (α, n) neutron emission rate of the test item

- $v_{j(\mu)} = \sum_{\mu=v}^{\infty} \binom{\mu}{v} P_{j\mu}$ is the μth factorial moment of the neutron emission distribution P by spontaneous fission

The experimental observables from the recorded pulse train can be obtained by looking at the signal triggered multiplets. In our case we limit to multiplets of order 0 and 1 and the experimental observables are the total count rate T_{exp} and the measured reals rate $R_{exp,m}$:

$$R_{exp} = \frac{(R+A) - A}{tf} = \frac{R_{exp,m}}{f} \tag{5.3}$$

Where

$$f = \int_{t_p}^{t_p + t_g} \frac{e^{-t/\tau}}{\tau} dt = e^{-t_p/\tau} \left(1 - e^{-t_g/\tau}\right) \tag{5.4}$$

and t is the measurement time. The f factor accounts for the finite duration of the trigger gate and the presence of a predelay. The given expression for f holds only for an exponential Rossi-alpha distribution (RAD).

In this work we applied the model equation (5.1) and (5.2) using the measured observables T_{exp} and $R_{exp,m}$ to derive the detection efficiency ε and the spontaneous fission rate F_s. The term α as well as the factorial moments of the neutron emission distribution associated to the assayed item were derived from the radionuclide composition of the sample. The f factor was obtained from the average of three values determined from the RAD: one from fitting the RAD with 2 exponentials, one from the observed RAD and correction for predelay assuming a 1 exponential function, one from the observed RAD and correction for predelay assuming a 2 exponentials function.

From the F_s one can determine the mass of the sample by dividing by F'_s, the number of spontaneous fission per second and per gram.

$$m_c = \frac{F_s}{F'_s} \tag{5.5}$$

5.4.2.2   Monte Carlo approach

We have additionally implemented a calibration approach where the number of the reals per spontaneous fission event ε_R is determined by Monte Carlo simulations [25]. This term implicitly accounts for the occupation factor associated to the experimental conditions as well as the multiplicity distribution associated to the spontaneous fission in the source. The composition of the radionuclide source must be known to determine ε_R.

We refer to [25] for a description of the Monte Carlo model. The approach relies on the following relation:

$$R_{exp,m} = \varepsilon_R \, m \sum_j f_{m,j} F'_{S,j} \tag{5.6}$$

where $f_{m,j}$ are the mass fractions for the radionuclide j.

Since the source composition may not be known at the moment when the Monte Carlo calculation is done, one could use a reference radionuclide (e.g. ^{240}Pu) for which the $\varepsilon_{R,REF}$ is calculated.

If we neglect the impact of the neutron energy distributions, in good approximation the number of reals per fission event is proportional to the average number of pairs per fission generated by the sources and we can therefore approximate the efficiency ratio as the ratio of the average number of pairs per fission:

$$\frac{\varepsilon_R}{\varepsilon_{R,REF}} \approx \frac{\frac{\left(\sum_j Q_j f_{m,j}\right)}{\left(\sum_j F'_{S,j} f_{m,j}\right)}}{\frac{Q_{REF}}{F'_{S,REF}}} = \frac{\frac{\left(\sum_j Q_j f_{m,j}\right)}{Q_{REF}}}{\frac{\left(\sum_j F'_{S,j} f_{m,j}\right)}{F'_{S,REF}}} \tag{5.7}$$

5.4.3 Results

The obtained masses m_c with the previously outlined procedures were compared with the nominal masses m_n of the measured samples. The obtained ratios m_c/m_n for the considered cases are given in Table 13 for the point model and Monte Carlo approaches. The quoted uncertainties result from count statistics on the net totals rate T_{exp}, the net reals rate $R_{exp,m}$ and on the reals per spontaneous fission event $\varepsilon_{R,REF}$ from Monte Carlo simulations, and have been obtained by first-order Taylor expansion-based error propagation..

The masses obtained by applying the point model are in good agreement with the nominal ones for the ^{252}Cf measurements both in the bare configuration and for the measurement with a drum. For the measurements with the ESARDA sources we observe a systematic overestimation of the mass. The reason of such a difference could be related to the fact for the ^{252}Cf the (α,n) contribution is negligible, when compared to the spontaneous fission term, while the contribution from (α,n) is significant for the PuO$_2$ sources and directly impacts the total count rate as indicated in Eq. (5.6). Given the open measurement geometry, the measured total count rate is also affected by neutron scattering in the surroundings and should be properly accounted for to correctly meet the point model conditions.

For the masses obtained by applying the Monte Carlo approach, the overall agreement between the obtained mass and nominal mass is very good. However, we observe that for asymmetrical measurement positions, such as position 7, deviations up to 26% are observed. Such a deviation is present both for the ^{252}Cf and the single pin single source setups, although the sign is not always consistent: the single source mass is overestimated in position 7 in drum 206 (Setup 4) and underestimated in drum 201, while the ^{252}Cf mass is always underestimated. The reason of these deviations is not yet understood. While in symmetrical measurements the contributions to the total and reals count rate from the two detectors are essentially the same, in an asymmetrical configuration one detector can contribute much more to the reals rate as, in the point model approximation, the reals rate is proportional to the square of the neutron detection efficiency [24]. Therefore the accurate position of the detector and source is even more important in an asymmetrical configuration.

TABLE 13. MC/MN VALUES FOR THE MEASURED COMBINATIONS OF DRUMS AND SOURCES AT DIFFERENT POSITIONS

Drum	SOURCE	Position	Setup	m_c/m_n Point Model	m_c/m_n Monte Carlo
None	^{252}Cf	1		0.95(1)	1.00(1)
	1 pin	1		1.21(3)	1.05(1)
201	^{252}Cf	1		1.03(1)	0.98(1)
		3		1.08(2)	0.98(1)
		7		1.04(1)	0.86(<1)
	1 pin	1		1.38(3)	1.02(1)
		2		1.46(5)	1.04(1)
		3		1.50(7)	1.05(2)
		5		1.36(3)	1.01(1)
		7		1.37(3)	0.94(1)
	7 pins	All	Setup 5	1.41(4)	1.00(1)
205	^{252}Cf	1		0.99(1)	0.97(1)
	7 pins	All	Setup 6	1.31(3)	0.98(1)
206	^{252}Cf	1		1.01(1)	0.99(1)
		7		1.01(1)	0.88(<1)
	1 pin	1	Setup 3	1.42(4)	1.02(1)
		2		1.49(5)	1.03(1)
		3		1.60(9)	1.07(2)
		3		1.56(8)	1.04(2)
		5		1.45(4)	1.01(1)
		6		1.41(3)	1.14(1)
		7	Setup 4	1.38(3)	1.26(1)
	7 pins	All	Setup 2	1.37(4)	1.00(1)

6   Calorimetric measurements at SCK CEN

6.1   Installation of the calorimeter

In September 2021, the calorimeter arrived by truck at SCK CEN, at the host building which was prepared in terms of electrical installation and data acquisition with remote access. Once inside the host building, the calorimeter was pushed to its final location using an air cushion system. Figure 29 provides some photographic impressions of the installation, as well as the calorimeter measurements with a drum in the measurement chamber, and a tent around the entire device for stabilization of temperatures. The tent around the calorimeter was constructed after the first tests without any radioactive materials indicated that the room temperature fluctuations were inducing large fluctuations in the recorded signals. The tent reduced the observed fluctuations considerably, but for the left and right block signals, they were still rather large. Exhausts were foreseen at both the left and right sides of the calorimeter, for the thermostatic baths. After completion of the required licenses, the foreseen measurement campaign at SCK CEN, within CHANCE WP3, could be initiated.

FIGURE 29. ARRIVAL OF THE CALORIMETER AT **SCK CEN** (TOP LEFT), UNLOADING WITH A CRANE (TOP CENTER), EMPTY DRUM AND CLAMP TO BE MOVED WITH THE OVERHEAD CRANE (TOP RIGHT), THE CALORIMETER AFTER INSTALLATION WITH THE EMPTY DRUM (BOTTOM LEFT), AND THE CALORIMETER IN THE CLOSED TENT DURING MEASUREMENT (BOTTOM RIGHT).

6.2 Measurements

The measurements performed with the calorimeter at SCK CEN included the same six setups as those investigated with the other NDA techniques listed in Table 6. Additionally, however, for the calorimetry, a specific set of baseline measurements was performed to quantify the "background" signal as well as possible. For the mock-up drums, we could do the baseline measurements without any radioactive material, which represents the ideal case. In practice, however, by no means a measurement can be performed on a drum that has the exact same thermal properties as the real radioactive waste drum to be measured. Hence, for enabling a more realistic assessment of uncertainties, additionally a baseline with empty calorimeter, and one with an empty drum were recorded as well.

After completion of the planned measurement campaign, the remaining time was used for performing multiple Joule effect measurements, targeting a more reliable calibration of the calorimeter. The different heat pulses, and corresponding sensitivity coefficients are discussed more in detail in Section 6.2.3. What is worth mentioning here, however, is that the baseline measurement for the Joule effect drum is likely the most representative for the real unconditioned waste drum (setup 1), as it consists of metal, which is the main type of material in the real drum, and has rather similar total weight. The Joule effect drum baseline is hence used as a baseline for the real unconditioned waste drum measurement (setup 1) in the remainder of this document. For a realistic assessment of uncertainties with respect to the baseline signal, the observed variation in baseline signal over all performed baseline measurements could be used, however. This would result in rather large uncertainty in the net signal, and hence building a quantitative relation between drum properties and baseline signal would be recommended in future.

An overview of the performed baseline measurements is provided in Table 14. Do note that the baselines with mock-up drums were repeated a second time after the measurements with radioactive sources, to check for potential drifts in the recorded signal. Differences in baseline, before and after measurements with radioactive sources, where however all consistent with the uncertainties, except for the central block, mock-up 205 baseline, where a significant but small systematic difference was observed (see Figure 32 and Figure 33).

TABLE 14. OVERVIEW OF THE BASELINE MEASUREMENTS PERFORMED AT SCK CEN, ADDITIONAL TO THE SETUPS MENTIONED IN TABLE 6 AND THE JOULE EFFECT MEASUREMENTS (SECTION 6.2.3).

Baseline	Description
Base A	Empty calorimeter
Base B	Empty drum inside calorimeter
Base 206	Mock-up 206, prior to measurements with sources
Base 206*	Mock-up 206, after measurements with sources
Base 201	Mock-up 201, prior to measurements with sources
Base 201*	Mock-up 201, after measurements with sources
Base 205	Mock-up 205, prior to measurements with sources
Base 205*	Mock-up 205, after measurements with sources
Base JE*	Joule effect drum baseline measurement at SCK CEN, used here as baseline for the real unconditioned waste drum

6.2.1 Raw data and noise correction

The raw data of the different recorded experiments is visualized in Figure 30 (the measurement and reference (noise) heatflow signals) and Figure 31 (the monitored temperatures). The heatflow signal mainly shows the large peaks obtained at times where the calorimeter was opened, or the thermal equilibrium of the measured object was not reached yet. Most remarkable is the long equilibration time for the first baseline with mock-up 206 that has, because of the mortar, by far the highest density and corresponding heat capacity. Peaks also occur at the end of the curves, as new experiments were sometimes only started just after modifying the contents of the calorimeter, and a single time in the middle (Base A&B) when two measurements were recorded within the same experiment.

The signal of the reference Peltier elements, that capture the noise in the measurement, is from this point on always subtracted from that of the measurement Peltier elements for noise correction. Initially, the reference signal was used unmodified, as recorded by the data acquisition system. After completion of the measurement campaign, and inspecting the raw data again, it was decided to introduce a multiplication factor for the reference signal, as the captured noise was very much correlated to the measurement signal, but clearly lower in magnitude, especially for the left and right blocks. For determining the multiplication factors, the stable time windows of all measurements were considered, and a linear regression was performed for each of the central, left and right blocks, with a single slope (= the multiplication factor) and a random intercept per measurement. This resulted in multiplication factors of 3.14, 3.96 and -0.0348 for the left, right and central blocks respectively (to be used as coefficients for V_i^{REF} in Equation 2.1). For the central block, the value is rather small, which indicates that noise correction is not really useful, and practically absent when using this coefficient. This does in fact make sense, as the reference Peltier elements of the central block are located below the ghost cell, and are further away from their corresponding measurement Peltier elements than in the left and right blocks. Moreover, the measurement Peltier elements of the central block are in between the measurement cell and ghost cell which is set up to react in a similar way to noise as the measurement cell, hence at least partly omitting the need for any noise correction. The resulting stable part of the signals is visualized in Figure 32.

The monitored temperatures in the left and right blocks always fairly quickly reached the target of 29°C. Again, in case of the first baseline with mock-up 206, it took considerably longer to heat up the mortar. The central block temperature was recorded, and behaved similarly, but is not part of the data exports due to technical issues, and hence not shown here.

If we compare the calorimeter tent temperatures, disregarding the Base A&B experiment (the tent was only installed afterwards), with the room temperature fluctuations, it is clear the former exhibits much smoother temperature changes. The observed range does however not appear to be very different, although the tent is consistently warmer, while both show much less fluctuations than the air temperature recorded at the meteo station. Occasionally, the gate or door of the room was opened, causing sudden peaks in the room temperature signal. These events are clearly buffered by the calorimeter tent, and although visible, have likely affected the measurements much less than if the tent would not have been there.

The stable parts of the heatflow signals in Figure 32 clearly illustrate the stability of the central block compared to that of the left and right block signals, which both received significant noise correction, while for the central block it is practically absent. Given the large fluctuations in the raw left and right block signals (both measurement and reference), an attempt was made to correlate them with the monitored temperature in the calorimeter tent, and the room temperature. While the correlation seemed useful for the central block, it did not seem very exploitable for further corrections of the left and right block signals because of occasional, until date unexplained, large

deviations from the temperature signal. Given the already small fluctuations of the central block signal, no further attempts were made towards a temperature-based correction.

What is furthermore apparent is that the signals are correlated over time, even though the updated noise correction removed most of that. This does have an impact on the effective sample size, and the corresponding uncertainty on the signal mean. For reliable estimation of the mean, it was therefore attempted to always collect four to five days of data after equilibrium was reached. With the updated noise correction, it seems however that two or three days may have been sufficient.
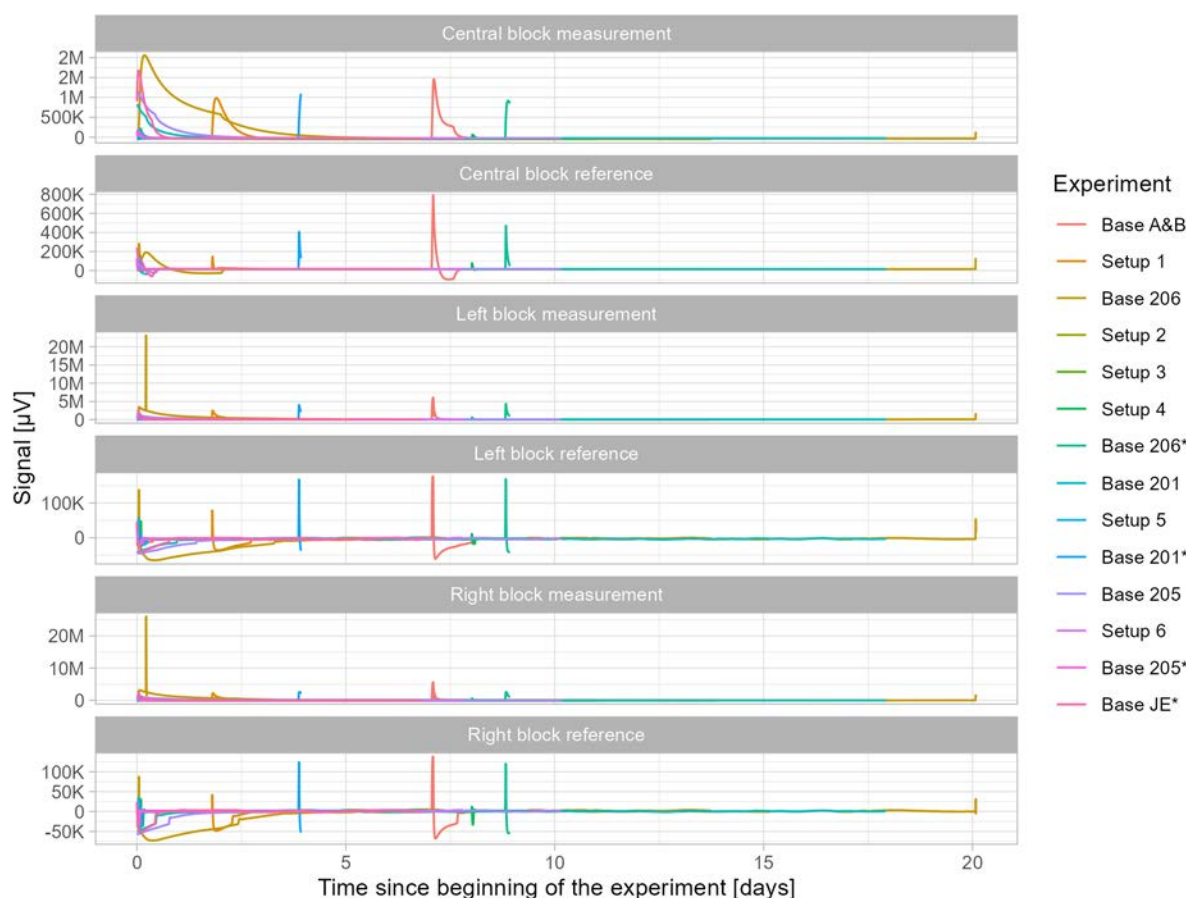

FIGURE 30. OVERVIEW OF THE RAW HEATFLOW DATA (VOLTAGES) RECORDED DURING THE DIFFERENT EXPERIMENTS. DO NOTE THAT THE STABLE PART OF THE ABSOLUTE SIGNAL IS ORDERS OF MAGNITUDE LOWER THAN THE OBSERVED PEAKS, AND HENCE THIS IS NOT CLEARLY VISIBLE IN THIS OVERVIEW FIGURE. THE STABLE PART IS VISUALIZED SEPARATELY IN FIGURE 32
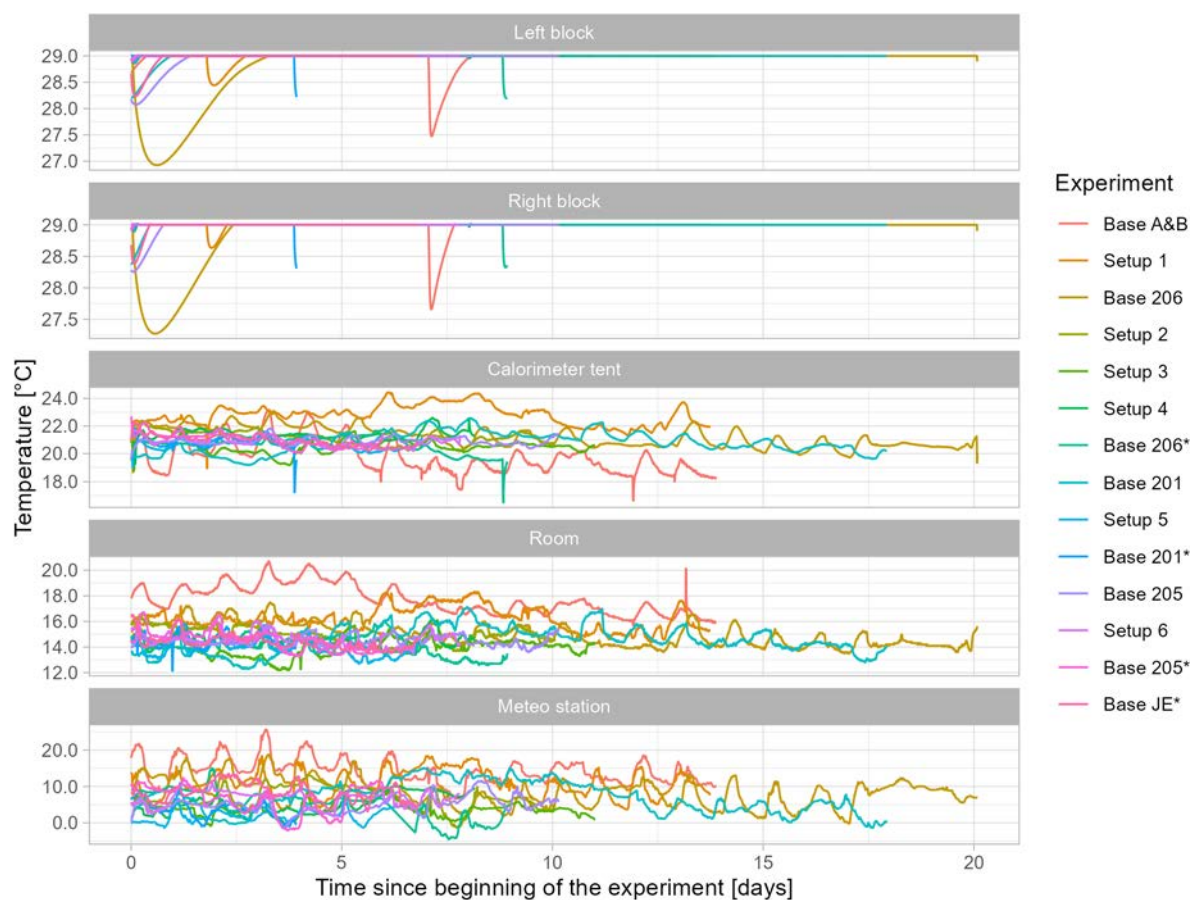
FIGURE 31. OVERVIEW OF THE RAW TEMPERATURE DATA RECORDED DURING THE DIFFERENT EXPERIMENTS. DO NOTE THAT THE CALORIMETER TENT TEMPERATURE IS THE ONE MEASURED BY THE CALORIMETER ITSELF, WHILE THE ROOM TEMPERATURES WERE RECORDED WITH EXTERNAL DEVICES. THE METEO STATION IS THAT OF HERENTALS, ABOUT 20 KM FROM SCK CEN.
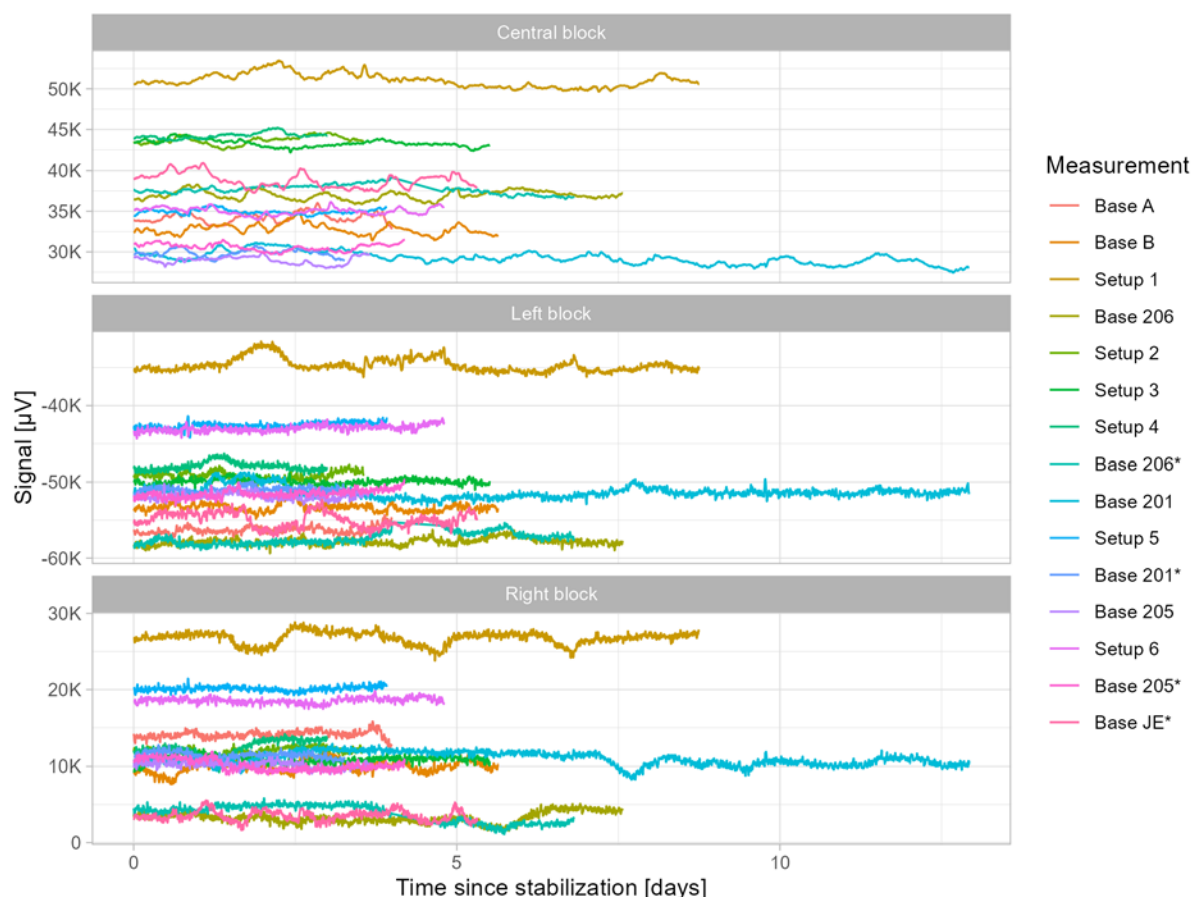
FIGURE 32. STABLE PART OF THE NOISE-CORRECTED HEATFLOW SIGNAL, FOR THE DIFFERENT BLOCKS AND MEASUREMENTS. FOR THE CENTRAL BLOCK, THE NOISE CORRECTION IS SO SMALL IT IS PRACTICALLY ABSENT.

6.2.2 Estimation of the mean and its standard error

To estimate the mean of the noise-corrected signal and its standard error, an exploratory analysis, using a series of different approaches, was performed. The average and standard deviation of the complete signal overestimate the uncertainty, as we are interested in the uncertainty on the mean itself. The classic standard error of the mean does not account for temporal correlation in the signal, and given the huge number of samples, collected over several days, it provides a clear underestimate of the uncertainty. The tested spectral density estimate of effective sample size proved not to be very robust, whereas the modified-Bartlett window and Tukey-Hanning window spectral variance estimation, and the batch means, overlapping batch means and iterative thinning approaches all provided similar results. Therefore, we decided to continue with the batch means approach (widely used method for estimating standard errors for Markov chain Monte Carlo), which results for practically all cases in a considerable reduction of uncertainty, compared to the plain standard deviation. The mean estimates and their corresponding uncertainties are visualized in Figure 33.

CHANCE

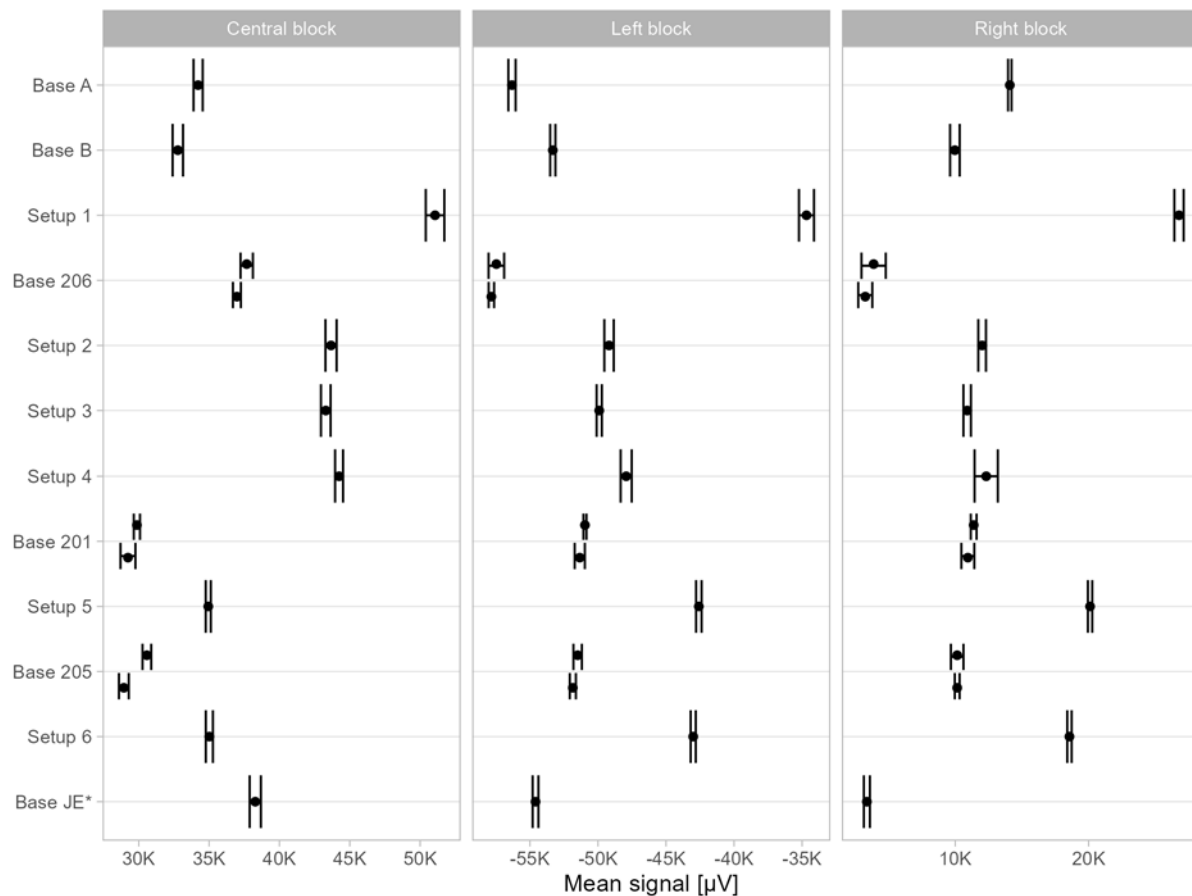| Title : Deliverable D3.3	Written:	List on Page 2		
Results of experimental investigation of calorimetry applicability	Organisation:	List on page 2	Version:	0
	Issued:	02nd April 2022	Page(s):	55

FIGURE 33. OVERVIEW OF ESTIMATED MEAN SIGNAL, AND ITS 95% CONFIDENCE INTERVAL, USING THE BATCH MEANS APPROACH, FOR THE DIFFERENT MEASUREMENTS AND THREE BLOCKS.

6.2.3 Joule effect measurements

After completion of the planned measurement campaign, the remaining time was used for performing multiple Joule effect measurements, targeting a more reliable calibration of the calorimeter. The joule effect drum baseline measurement was introduced before, as it seems to be the most adequate for representing the real unconditioned waste drum baseline. Next to the baseline measurement, a series of joule effect pulses was performed, at 500, 375, 250, 200, 150, and 50 mW. Each thermal power was maintained for 72 hours, after which the next pulse was started. After the first pulse, however, 60 hours of standby time was used to check also with this drum for any potential drift in the baseline signal, which again seemed to be absent.

Additional to the pulses measured at SCK CEN, the raw measurement data from the 500 mW pulse performed at KEP, and the corresponding baseline, before transport of the calorimeter, was analysed in the exact same way, and added to the calibration dataset.

For enabling a first interpretation of the measured net voltages of all experiments, in terms of thermal power, a classic simple linear regression exercise was performed without any intercept to estimate a sensitivity coefficient for every block individually, and the sum of the three signals, with results summarized in Table 15 and Figure 34. A

more complex calibration exercise can in theory be performed here (even if just by framing this as a prediction of thermal power in function of net voltage, and then account for prediction error), and the mock-up drum measurements with reference sources could be leveraged as well for this purpose, but this was considered sufficient here given the scope of the current document. A more detailed analysis will be performed within deliverable 3.4.

TABLE 15. OVERVIEW OF SENSITIVITY COEFFICIENTS OBTAINED FROM SIMPLE LINEAR REGRESSION WITHOUT INTERCEPT.

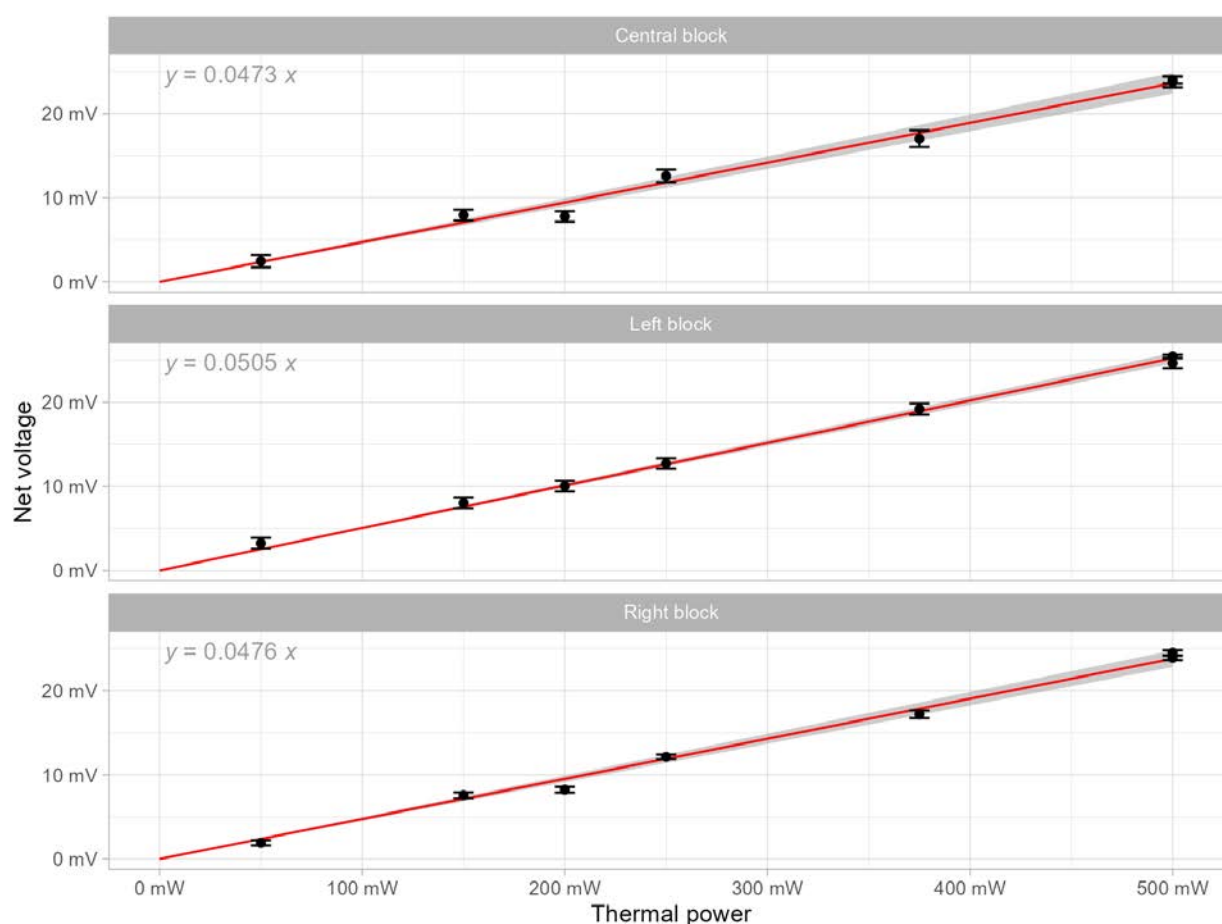| Sensitivity for	Estimate (mV/mW)	Standard error
Left block	50.5	0.51
Right block	47.6	0.81
Central block	47.3	1.02
Total signal (sum)	145.4	1.82

FIGURE 34 OVERVIEW OF THE SIX JOULE EFFECT MEASUREMENTS, AND THE CORRESPONDING LINEAR MODEL FIT FOR THE THREE CALORIMETER BLOCKS.

CHANCE

Title : Deliverable D3.3	Written:	List on Page 2	
Results of experimental investigation of calorimetry applicability	Organisation:	List on page 2	Version: 0
	Issued:	02nd April 2022	Page(s): 57

6.2.4   About the detection limit and minimum detectable power

Given the mean values and corresponding standard errors from the different measurement setups, joule effect pulses, and corresponding baselines, we are able to do some calculations of detection limits, under the assumption that the standard error does not depend on the mean. For obtaining a decision threshold, we can for instance calculate the 0.975 quantile of the different baseline signal means, only allowing for a 2.5% probability that we would decide heat is generated within the measurement chamber, while this is in fact not the case (false alarm risk, or "α" risk). Following the calculation of the decision threshold, we can look for the gross voltage mean, where the 0.025 quantile would equal that decision threshold, only allowing for a 2.5% probability that we would conclude no heat is generated based on the decision threshold, while this is in fact not the case (non-detection risk, or "β" risk). The difference between that gross voltage mean and the baseline voltage mean then gives the detection limit in terms of the net voltage and is calculated as the sum of the standard errors multiplied by a coverage factor of 2.

To go a step further, and estimate a minimum detectable power, one could assume the sensitivity coefficients to be deterministic, and not account for systematic error. Here, however, we use a more conservative approach, and use the 0.05 quantile of the sensitivity coefficients, based on the numbers mentioned above, to come up with a simple conservative estimate of the minimum detectable power.

The results of both characteristic limits are summarized in Table 16, for the individual blocks, for two cases: One where we consider that a representative baseline measurement is available, which is consistent with the rest of this document. For the other case, we assume no representative baseline measurement is available, and we use the standard deviation of all baseline signal means instead. For the representative baseline case, the minimum detectable power is at best in the range of 5 to 15 mW, while for the more uncertain measurements, it increases to 20 to 40 mW. For the second case, however, the uncertainty in the baseline increases drastically, and the minimum detectable power ends up in the range of 100 to 200 mW.

TABLE 16. OVERVIEW OF THE CHARACTERISTIC LIMIT ESTIMATES BASED ON THE DIFFERENT PERFORMED MEASUREMENTS. THE CALCULATION WAS PERFORMED FOR ALL MEASUREMENTS, AND WE PROVIDE THE MINIMUM AND MAXIMUM VALUES HERE.

Characteristic limit	With representative baseline			With unknown baseline		
	Left	Right	Central	Left	Right	Central
Detection limit (μV)	280 - 1200	350 - 1800	600 - 1400	5200 - 5700	8800 - 9600	8200 - 8800
Minimum detectable power (mW)	5.5 – 23	7.5 - 39	13 - 30	100 - 110	190 - 210	180 - 190

6.3   Results

For the preliminary total power estimates, we used the sensitivity coefficients and standard errors presented above. As the repeated baseline measurements with the mock-up drums were mostly consistent, we just used the one performed prior to the introduction of sources to obtain the net voltages to use for estimating the total power, except for the last experiment with mock-up 206, which was clearly closer in time to the baseline performed afterwards. Finally, we also made the assumption that 100% of the radiation, in all these experiments, deposits its

energy within the measurement chamber of the calorimeter, so that the theoretical potential efficiency for the calorimeter is 100% (see Section 6.4 for more details). The corresponding results in terms of thermal power are provided in Figure 35.

For setup 1, it seems the calorimeter suggests a somewhat larger total power, than our a priori estimate. As this is a real drum, we do not exactly know the true values here of course, and the full probabilistic modelling exercise for deliverable 3.4 will point out if our best estimate will indeed shift to larger values, given the different measurements performed. That said, however, it seems that the central block on itself does suggest a total power close to the a priori estimate, and given its stability compared to the other blocks, this may very well be our best estimate for the real drum at this point. Also, we used here our best estimate for the real drum baseline (that of the joule effect drum), which may still not be very adequate. A different baseline may shift the calorimeter-based estimates up or down. An approach could be to consider a much more uncertain baseline for the real drum, which would result in larger confidence intervals, potentially capturing our a priori estimate as well.

For setups 2 to 6, where mock-up drums were used, it seems most results are consistent with the a priori estimate, or at least those of the combined signal. The a priori estimate, in this case, is rather certain given the fact that we used certified reference sources and accounted for the decay. The only remarkable thing is that the individual blocks seem to exhibit some bias here, which seems to be compensated for, when combining all of them in the total signal. When considering the fact that the relative amounts of heatflow through the different blocks may depend on the object measured, and the location of heat sources, then this does make sense however.
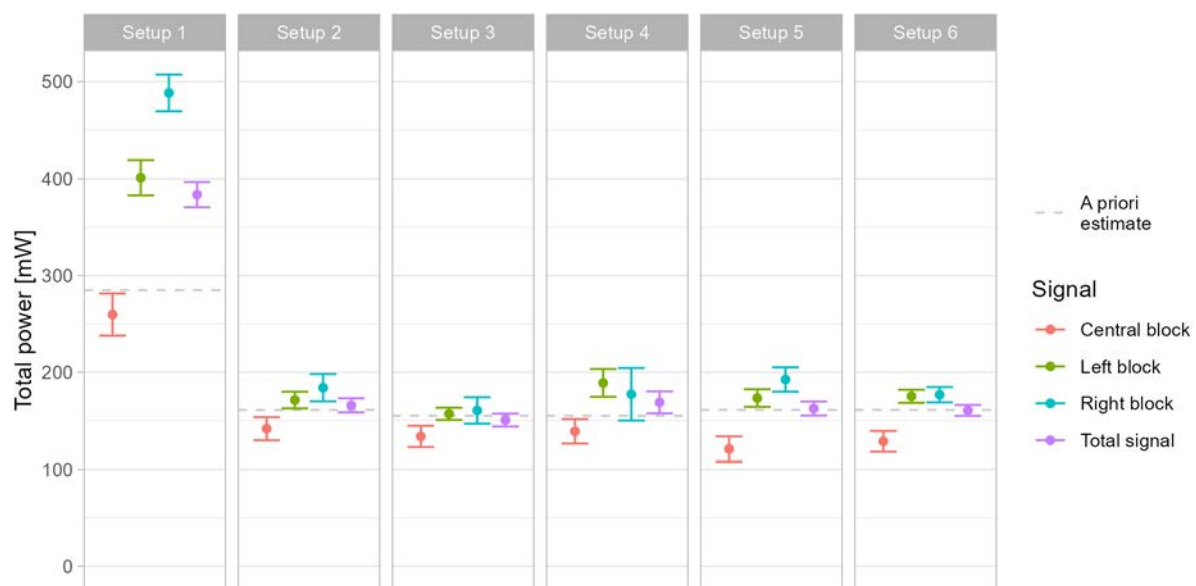

FIGURE 35. PRELIMINARY TOTAL POWER ESTIMATES, AND COMPARISON WITH OUR A PRIORI ESTIMATES, FOR THE DIFFERENT INVESTIGATED SETUPS, AND DERIVED SENSITIVITY COEFFICIENTS.

6.4   Associated numerical studies

Based on different calculations for the gamma and alpha radiation of the radioisotopes considered in the measurements at SCK CEN, as well as the position of sources within the mock-ups, it was concluded that the efficiency of the calorimeter in terms of capturing the generated heat within the measurement chamber, was practically 100%. Therefore, for the interpretations of the calorimeter measurements above, as well as the more comprehensive probabilistic modelling exercise later on, we assume there is no significant escape of radiation nor heat.

An example of the results concerning deposition of energy is given below for the real drum measured at SCK CEN. This drum consists mainly of Pu isotopes and Am-241. Homogeneous segments or central point sources were considered by [64] for introducing some uncertainty on the efficiencies on a segment bases, in an exercise looking at segmented gamma scanning. The corresponding deposition of heat in the calorimeter was simulated, in order to quantify the potential maximum efficiency of the calorimeter for the different cases. The energy deposited by gamma particles is displayed in Figure 36 and Figure 37, for the homogeneous segment and central point source cases respectively.

The corresponding potential gamma heat detection is about 90%, with a decrease to about 80% at the top and the bottom of the drum (Figure 38). However, taking into account the fact that the composition mainly includes alpha emitters responsible for > 99% heat deposition, the final potential heat detection is close to 100% and does not depend on the position or distribution of the source (Figure 39). Hence, it is assumed throughout this document, and the follow-up work, that the calorimeter efficiency is 100% for the real unconditioned waste drum measured at SCK CEN. For the reference sources and mock-up drums, we came to similar conclusions, and work with the same assumption.
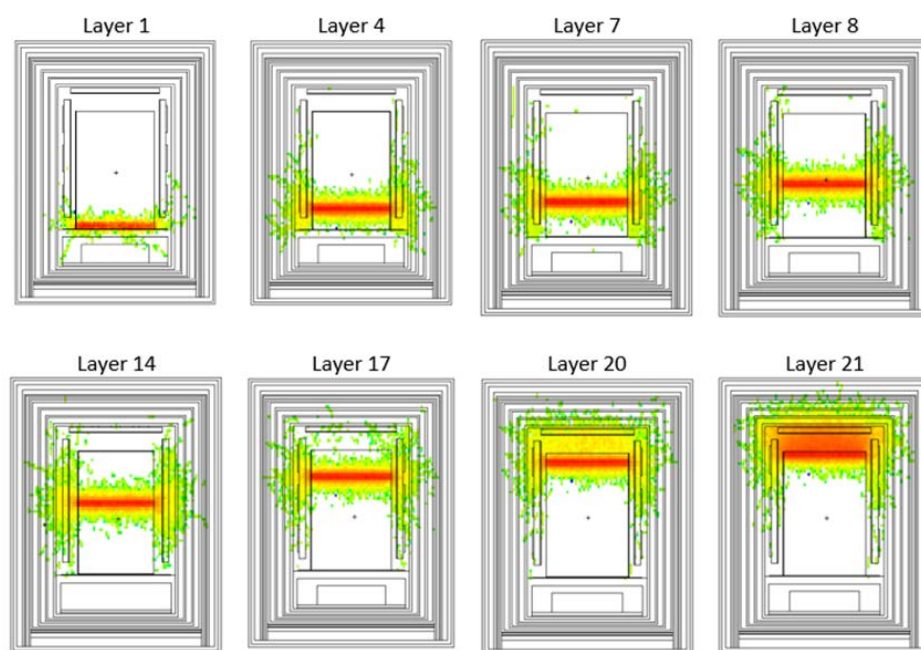
FIGURE 36. ENERGY DEPOSITION OF GAMMA PARTICLES, FOR A SELECTION OF HOMOGENEOUS SOURCE SEGMENTS, FOR THE REAL UNCONDITIONED WASTE DRUM MEASURED AT SCK CEN.
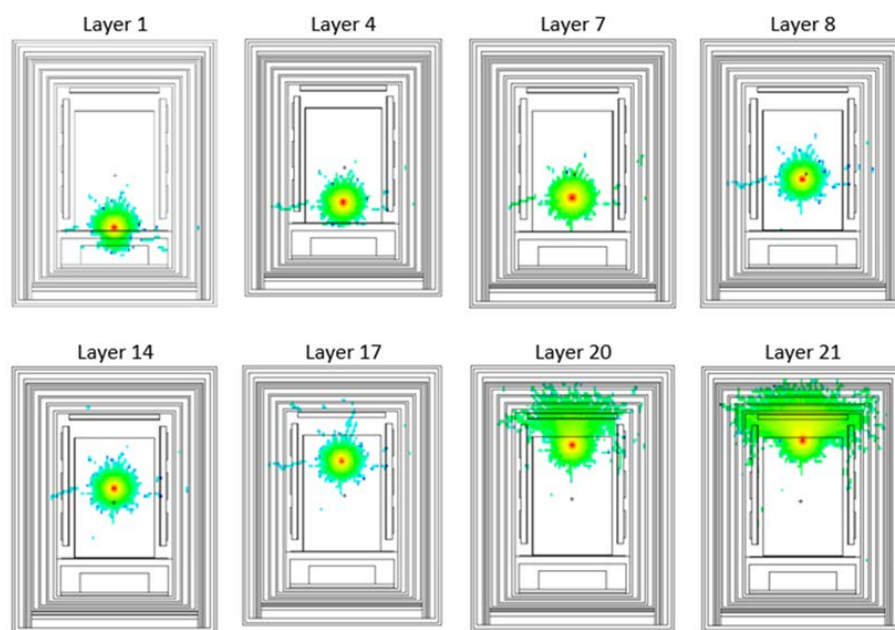

FIGURE 37. ENERGY DEPOSITION OF GAMMA PARTICLES, FOR A SELECTION OF POINT SOURCES, FOR THE REAL UNCONDITIONED WASTE DRUM MEASURED AT SCK CEN.
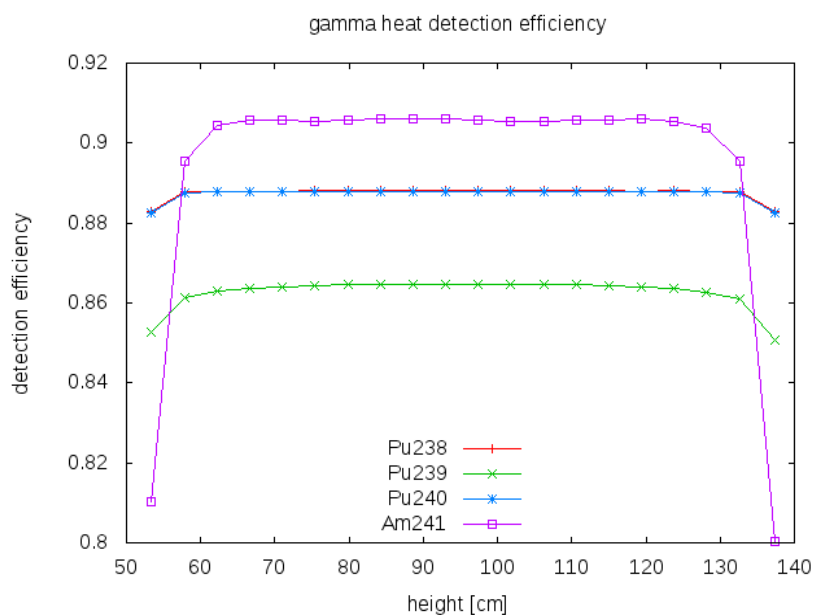
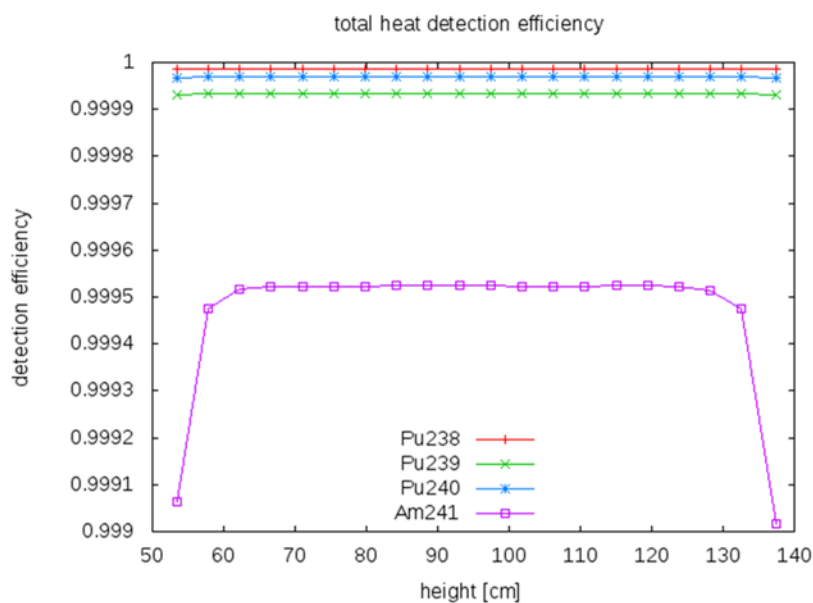**FIGURE 38. GAMMA HEAT DETECTION FOR DIFFERENT POSITIONS OF THE SOURCE LAYER.**

FIGURE 39. TOTAL HEAT DETECTION FOR DIFFERENT POSITIONS OF THE SOURCE LAYER.

7 Conclusion

The gamma spectroscopy and passive neutron coincidence counting (PNCC) measurements may show punitive uncertainties due to radiation attenuation effects in dense waste matrices, when the position of plutonium inside the waste package is not known, which is the case for most heterogeneous technological waste. We observed for instance a discrepancy larger than a factor 10 between the PNCC signals, depending on source position inside a 220 L concrete mock-up drum. In this frame, calorimetry measurements have shown to be far less sensitive to coupled matrix and source position effects. A more detailed analysis of all uncertainties in the performed measurements and calculated efficiencies, possibly also resulting in more accurate estimates, and a corresponding theoretical assessment of a series of different isotopic vectors, will be provided in D3.4, in view of further quantifying the usefulness of calorimetry for 200L radioactive waste drums.

Concerning the new calorimetric measurement technique added to improve gamma and neutron measurements, we can highlight the following lessons learned that will be extremely valuable for a future application:

– The central block misses a part of the heat emitted by the drum in regards of how the calorimeter is calibrated.
– Therefore it is important to take into account the heat going through the centre, right and left parts of the calorimeter considering the way how the calorimeter is calibrated.
– The calorimeter is very sensitive to the fast room temperature variation and the thermal inertia does not make possible to compensate it.
– The reference system (Peltier modules) on the left and right does not see the perturbation coming from the outside in the same amplitude than the measurement system (Peltier modules). When processing the data measured in SCK CEN, a correction coefficient was applied on the reference signals to follow the same amplitude of measurement signal, which gives good results without bringing a bias on the true mean measured power.
– Baseline determination is very important for real drums. For mock-up drums it is very precise as we introduce Pu samples in the same drums used for baseline measurements, but for real drums baseline depends on the mass and thermal conductivity of the waste matrix. Therefore, building a quantitative relation between drum properties and baseline signal would be recommended in the future.
– The minimum detectable power can be as low as 5 to 15 mW under good conditions, meaning a representative baseline is available, temperature fluctuations are limited, and the measurement time is sufficiently long.
– On the other hand, without a representative baseline, the minimum detectable power quickly increases towards values in the range of 100 to 200 mW.

The improvements necessary to study large waste drums and improve the detection limit would be to:
o Adapt the ghost cell to the mass and thermal conductivity of the drum.
o Have a better differential measurement for the left and right blocks, aiming at similar amplitudes of the measurement and reference signal variations with room temperature.
o Insulate the drum more from the outside and let the heat only go through the central block (no more measurements by the right and left will then be necessary), which will also simplify the manufacturing of the calorimeter.

8 References

[1] Calorimeter delivery, CHANCE Deliverable D3.2 related to Task 3.2 (2020).

[2] G. Jossens, C. Mathonat, J.-C. Hubinois, A. Godot, F. Bachelet, HEAT FLOW MEASURING DIFFERENTIAL CALORIMETER" Patent XD13897IM, EP 14 700408.9 (2015)

[3] Applicability of Calorimetry to Real Waste Characterisation, CHANCE Deliverable D3.1 related to Task 3.1 (2018).

[4] T. Marchais, B. Pérot, C. Carasco, et. al., Detailed MCNP Simulations of Gamma-Ray Spectroscopy Measurements With Calibration Blocs for Uranium Mining Applications, IEEE Transactions on Nuclear Science 65, 2533-2538 (2018).

[5] J. L. Parker, The Use Of Calibration Standards And The Correction For Sample Self-Attenuation In Gamma-Ray Nondestructive Assay, Los Alamos National Laboratory, LA-10045 (1984).

[6] C.J. Werner (editor), "MCNP Users Manual - Code Version 6.2", LA-UR-17-29981 (2017).

[7] http://physics.nist.gov/cgi-bin/Star/compos.pl?matno=144

[8] Recommandations en vue de l'étalonnage d'un poste de mesure pour la détermination de caractéristiques radioactives de colis de déchets par comptage neutronique passif, Norme Française NF M 60-315.

[9] Buecherl, T., Kaciniel, E., Lierse, C. H. 1998.Synopsis of gamma scanning systems - comparison of gamma deter-mining systems and measuring procedures for radioactive waste packages. European Network of Testing Facilities forthe Quality Checking of Radioactive Waste Packages, Report WG-A-01, September 1998

[10] ISOCS/LabSOCS Detector Characterization Report. Canberra Sales Order #49913. Detector Model BE3830. S/N B15061. Canberra.

[11] Genie 2000 Spectroscopy Software - Customization Tools. Canberra Industries, Inc.

[12] Model S575 - PC/FRAM Isotopics - Software - User's Manual (9231022B V4.4). The Regents of the University of California.

[13] https://www.mirion.com/products/wm3400-passive-neutron-slab-counter. Last accessed 28/04/2021

[14] [Boogers E., et al., 2019. "Improved electronics for 3He based neutron counters". Proceedings of the 2019 ANIMMA conference.

[15] Canberra, 2006. "Model JSR-12 Neutron Coincidence Analyzer User's Manual", Canberra Industries Inc.

[16] GBS, 2021. https://www.gbs-elektronik.de/media/download_gallery/mca527_neutron.pdf. Last accessed 28/04/2021

[17] Bignan G. et al., 1995. "Proposal of an intercomparison exercise for the characterization of waste containing plutonium by NDA methods." Working document of the 17th annual ESARDA meeting.

[18] Bignan G., et al., 1996. "Preparation of standard drums for the calibration of nuclear waste measuring facilities. Final report". CEA note technique NT-SSAE-LSMR 98/0016.

[19] A. Verbruggen, R. Garcia-Galan, Certification of BC1413, GE/R/SIM/7/98 June 1998, IRMM Stable Isotope Measurement Unit

[20] https://www.python.org/

[21] https://docs.spyder-ide.org]

[22] R. Dierckx & W. Hage (1983) Neutron Signal Multiplet Analysis for the Mass Determination of Spontaneous Fission Isotopes, Nuclear Science and Engineering, 85:4, 325-338,

[23] W. Hage & D.M. Cifarelli Nucl. Sci & Eng. 89 (1985) 159-176

[24] D.M. Cifarelli & W. Hage Nucl. Instr. & Meth. A251 (1986) 550-563

[25] A. Borell a, et al., Neutron Coincidence Measurements and Monte Carlo Modelling of Waste Drums Containing Reference Nuclear Material, EPJ Web Conf. 253 07001 (2021), DOI: 10.1051/epjconf/202125307001

[26] Laloy E, Rogiers B, Bielen A, Boden S. 2021. Bayesian inference of 1D activity profiles from segmented gamma scanning of a heterogeneous radioactive waste drum. Applied Radiation and Isotopes, Volume 175, 109803, ISSN 0969-8043, https://doi.org/10.1016/j.apradiso.2021.109803.